LMU LUDWIG-MAXIMILIANS-UNIVERSITÄT
TECHNISCHE UNIVERSITÄT MÜNCHEN TUM

Helmholtz Zentrum München
Institute of Computational Biology

Bachelorarbeit
in Bioinformatik

Development of a Program for Automatic Quantification of Mammospheres in Limiting Dilution Assays

Linda Maria Leidig

Aufgabensteller:	Prof. Dr. Dr. Fabian Theis
Betreuer:	Felix Buggenthin, Dr. Carsten Marr
Abgabedatum:	01.10.2013

Ich versichere, dass ich diese Bachelorarbeit selbständig verfasst und nur die angegebenen Quellen und Hilfsmittel verwendet habe.

01.10.2013 _____

Linda Maria Leidig

Abstract

In 2011 breast cancer, which can occur in different aggressive forms, was the ninth most common cause of dead in Germany. Breast cells with stem cell potential are an important discovery of cancer research in the past few years. These cells are able to differentiate into various cell lineages and self-renew, meaning that at least one of the two daughter cells, which arise from cell division, has stem cell properties. The more tumour cells have stem cell properties, the more aggressive is the tumour. A quantification of the tumourigenicity by determination of the proportion of cells with stem cell properties is preferable. Moreover, the identification and study of stem cells is difficult to realise *in vitro* since destroying a mice's immune system and implanting a cancer cell is expensive. Therefore, an *in vitro* assay was developed that shows that cells with stem cell properties, which are cultured in a specific medium, form cell colonies (mammospheres) after five to seven days. The sphere forming rate suggests the aggressiveness of the cancer type. So far, the sphere forming rate is either determined by division of the number of mammospheres at the experiment end by the number of breast cells at the experiment start or by a so called Limiting Dilution Analysis. Both approaches comprise drawbacks mostly based on the experimental difficulty to fill an exact number of cells into a particular experimental volume.

Here, we developed an alternative method to determine the sphere forming rate. It is based on the division of the number of mammospheres at the experiment end by the number of cells at the experiment start like the first approach. Microscopic images of the cells are taken at several time points in constant time intervals. In contrast to the aforementioned methods, we determine the number of mammospheres and cells automatically with the help of several image processing methods. This approach allows the precise determination of the cell density and sphere forming rate. To enable an application of the method by our biological partner, we implemented an image processing pipeline on the basis of the program CellProfiler and validated it manually. The pipeline was applied to an experiment of Dr. Scheel's group at the ISF, Helmholtz Centre Munich, comprising two different breast cancer cell lines and compared to the results of the classical Limiting Dilution Analysis. The results of the automatic analysis confirmed different levels of aggressiveness between the different cell lines by trend.

The automatic method developed in this work is a first step towards a robust, automatic determination of the sphere forming rate. It is possible to use the method in a high-throughput manner, e.g. to study the impact of small molecules on the sphere forming rate. Moreover, analysing all images of a movie enables further findings both in the context of determining the sphere forming rate and the dynamics of sphere forming.

Zusammenfassung

Im Jahr 2011 war Brustkrebs, der in unterschiedlich aggressiven Formen auftritt, die neunthäufigste Todesursache in Deutschland. Eine wichtige Entdeckung der Krebsforschung der letzten Jahre sind Brustzellen mit Stammzelleigenschaften. Diese Zellen sind in der Lage, in verschiedene Zelltypen zu differenzieren und sich selbst zu erneuern, was bedeutet, dass mindestens eine der beiden Tochterzellen, die bei der Teilung entstehen, ebenfalls Stammzelleigenschaften hat. Je mehr Zellen eines Tumors Stammzelleigenschaften haben, desto aggressiver ist dieser. Wünschenswert ist eine Quantifizierung der Tumorigenität durch die Bestimmung des Anteils der Zellen, die Stammzelleigenschaften haben. Die Identifizierung und Untersuchung der Stammzellen *in vivo* ist schwierig, da es sehr aufwendig ist, zunächst das Immunsystem der Mäuse zu zerstören und die Krebszelle dann einzupflanzen. Daher wurden verschiedene *in vitro* Verfahren entwickelt, bei denen beobachtet werden kann, wie Zellen mit Stammzelleigenschaften, die lose in einem bestimmten Medium kultiviert werden, nach fünf bis sieben Tagen Zellkolonien (Mammosphären) bilden. Die Rate, mit der Brustkrebszellen Sphären bilden, lässt darauf schließen, wie aggressiv die Krebsart ist. Bislang wird die Rate der Sphärenbildung entweder durch Division der Anzahl der Mammosphären am Ende des Experiments durch die Anzahl der Brustzellen zu Beginn bestimmt oder durch die sogenannte Limiting Dilution Analyse. Bei beiden Ansätzen kommt es jedoch zu Problemen, die hauptsächlich darauf basieren, dass es experimentell schwierig ist, eine genaue Anzahl an Zellen in ein bestimmtes Versuchsvolumen zu füllen.

Im Rahmen dieser Arbeit haben wir eine alternative Methode entwickelt, um die Rate der Sphärenbildung zu bestimmen. Sie basiert wie der erste Ansatz darauf, die Anzahl der Mammosphären am Ende des Experiments durch die Anzahl der Zellen zu Beginn des Experiments zu teilen. Die Zellen werden an unterschiedlichen Zeitpunkten in gleich großen Zeitintervallen mikroskopisch fotografiert. Im Gegensatz zu den oben beschriebenen Methoden bestimmen wir die Anzahl der Mammosphären und Zellen automatisch mit einer Reihe von Bildverarbeitungsmethoden. Dieser Ansatz erlaubt uns eine genaue Bestimmung der Zelldichte und der Rate der Sphärenbildung. Um die Anwendung der Methode für unseren biologischen Partner zu ermöglichen, haben wir eine auf dem Programm Cellprofiler basierende Bildverarbeitungspipeline implementiert und diese manuell validiert. Die Pipeline wurde auf ein Experiment aus der Arbeitsgruppe von Dr. Scheel, ISF, Helmholtz Zentrum München, mit zwei verschiedenen Brustkrebszelllinien angewendet und mit den Resultaten klassischer Limiting Dilution Analysen verglichen. Das Ergebnis der automatischen Analyse bestätigte tendenziell eine höhere Aggressivität der einen Zelllinie gegenüber der anderen.

Die in dieser Arbeit entwickelte, automatische Methode ist ein erster Schritt auf dem Weg zur robusten, automatischen Bestimmung der Rate der Sphärenbildung. Die Methode kann als Hochdurchsatzmethode verwendet werden, um z.B. den Einfluss verschiedener Moleküle auf die Rate der Sphärenbildung zu untersuchen. Außerdem ermöglicht die Analyse aller Bilder eines Films weitere Erkenntnisse, sowohl im Hinblick auf die Bestimmung der Rate als auch auf die Dynamik der Sphärenbildung.

Contents

List of Figures

List of Tables

1 Introduction

1.1 Human Mammary and Cancer

In 2011 breast cancer ranked ninth in the causes of dead statistics in Germany and is the most frequent carcinosis of womankind [13, 33]. Different types of breast cancer with different properties exist. The tumours can grow into ambient tissue, which is called invasive [36]. Non-invasive cancer types stay in one type of tissue. Some cancers metastasize, meaning the spreading into other parts of the body. Cancer can also occur recurrently after therapy, called relapse [10]. These different traits render the treatment of cancer very complex. Hence, the interest in breast cancer research expanded in the past few years.

Breast cancer originates in different cell types of the breast epithelium, which is divided into the luminal and myoepithelial or basal cell lineages [54]. The former is subdivided into ductal and alveolar cells. Ductal cells create a branched ductal system surrounded by myoepithelial cells that form a continuous layer. Since alveolar cells are responsible for milk production, they are developed during pregnancy. Alveolar cells are also surrounded by myoepithelial cells forming a more open network [34]. Myoepithelial cells have myofibers. Thus, they are able to contract the epithelium formed by the luminal cells, which is why they are important for breastfeeding [54]. The described breast structure is shown in Figure 1.

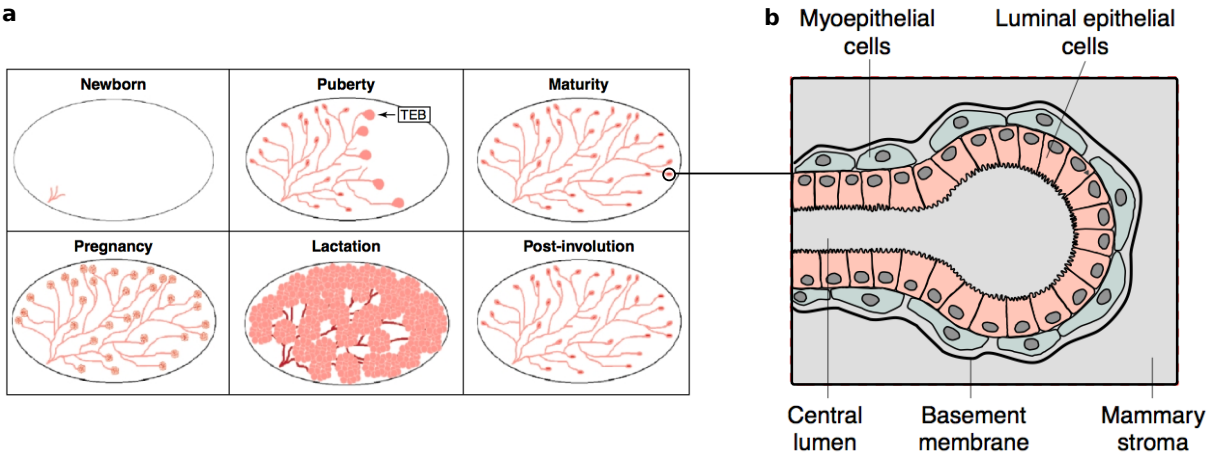

Figure 1: Development of the human mammary structure. a) The female breast is composed of a branched ductal system. During different stages of development this system shows different characteristics. During puberty the ductal system grows, building terminal end buds (TEBs), which are able to end in both luminal and myoepithelial cells. After puberty, at maturity, the TEBs are replaced by end buds. A second extension comes along with pregnancy. Alveolar cells are generated during pregnancy to provide a secretory phenotype during lactation. After breastfeeding i.e. post-involution the ductal system degenerates. b) The detailed view shows an end bud, which exists at maturity. The luminal epithelial cells are surrounded by myoepithelial cells and enclose the central lumen. The ducts or end buds are surrounded by a basement membrane enclosed by mammary stroma. Image adapted from [46].

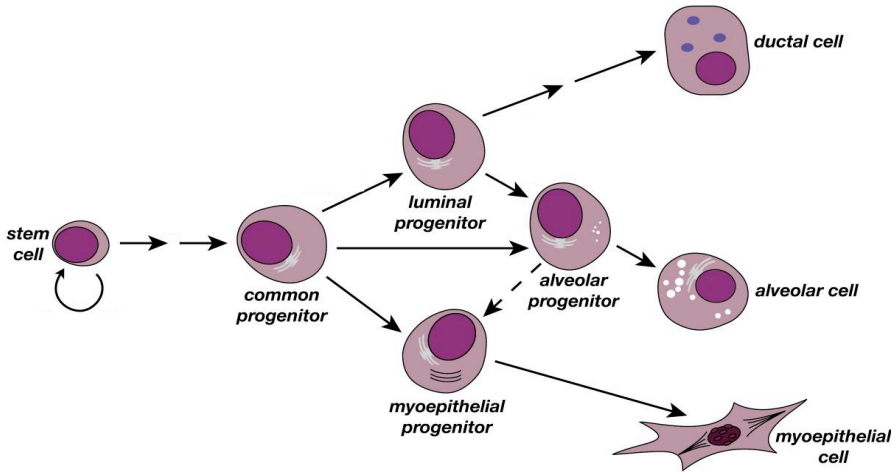

Figure 2: Differentiation hierarchy of mammary epithelium. The multipotent stem cell differentiates into the three cell lineages, ductal, alveolar, and myoepithelial (or basal) cells. Alveolar progenitors may achieve bipotential capacity during pregnancy. Image adapted from [54].

Different types of tumours show differing levels of aggressiveness. That means that the tumours grow with different speed and metastasize to different extent. If myoepithelial cells turn into tumour cells, they have mesenchymal properties. Since myoepithelial cells are located at the edge of the epithelium (see Figure 1b), they can translocate into the surrounding connective tissue, which serves as scaffolding [52]. This process is referred to as epithelial to mesenchymal transition [5]. In the connective tissue it is easier for the cells to leave their place of origin and pass over into the blood system, by which they are transported into other tissues (metastazation) [27]. Therefore, these cells metastasize frequently, which makes them very aggressive. Less aggressive tumour cells arise from luminal cells. Since abnormal luminal cells retain epithelial properties they metastasize more rarely.

It was shown that the three different cell lineages, namely ductal, alveolar, and myoepithelial cells, arise from a single stem cell, where a hierarchical differentiation model is assumed (see Figure 2) [54]. These stem cells are important for both organ development and maintenance of tissue homeostasis, which stands for the reproduction of breast cells to ensure the balance between the cells that die and the ones which are newly produced. The massive extension of the human mammary tissue during puberty and pregnancy can also be explained by the existence of stem cells. Besides the differentiation into the three cell lineages, the main property of stem cells is the ability of self-renewal. When a stem cell divides, the process is referred to as self-renewal if at least one of the new cells has stem cell characteristics.

1.2 From Stem Cells to Cancer

The relation between breast stem cells and cancer cells is mainly based on the self-renewal capacity of stem cells [30]. In [48] the assumption was made that a mutation, affecting the self-renewal process, leads to abnormal cells due to parallels in the self-renewal properties of normal stem cells and tumour cells. These cancer cells with stem cell properties are also called cancer stem cells (CSC) [5]. Given these attributes, breast stem cells serve

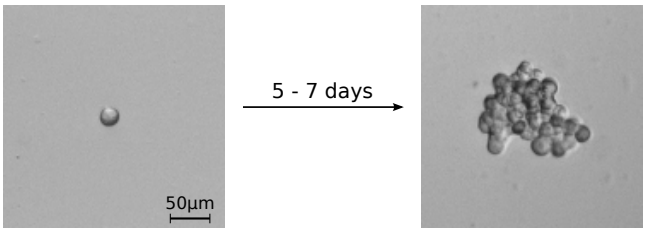

Figure 3: Bright field image of a breast cell (left) and a mammosphere (right). After five to seven days in suspension breast cells with stem cell properties form non-adherent mammospheres. These cells are called sphere-initializing cells.

as a good model system to learn more about the processes involved in carcinogenesis [30]. For that purpose, the different sub-populations of stem cells and their progenitors must be identified. Usually the identification of specific cell types is done by using cell-surface markers, which bind specifically on the basis of the cell's surface receptors and can be detected afterwards. Due to a lack of appropriate surface markers for different populations of breast cells and progenitors, it is helpful to have an *in vitro* assay that allows propagation in an undifferentiated state and enrichment of stem cells [30].

1.3 Detecting Breast Cells with Stem Cell Properties in Vitro

One approach to satisfy the aforementioned needs is the mammosphere assay [30]. By putting single breast cells into a serum-free suspension containing growth factors, some of the cells form colonies after about seven days (see Figure 3). These colonies are called mammospheres. If the spheres originate from cancer cell lines, they are also called tumourspheres [49]. Only one cell is needed to form a sphere without required aggregation or cell-cell contact. This sphere-initializing cells seem to be multipotent stem cells so that forming the mammosphere is caused by the capability of self-renewal [30].

In vivo breast cells are adherent, which means that they need to grow on top of a basement membrane. Notably they would not be able to survive without this basement membrane, which is why treated well plates are used for *in vitro* culturing. To avoid adherence, untreated low attachment well plates are used so that the breast cells are forced to grow in anchorage independence [30]. Only stem cells and tumourigenic cells are able to grow adherent, which makes this assay very important in the breast cancer research.

Making a suspension of single cells conserved by passaging from mammospheres and repeated incubation for about seven days entails second degree or secondary mammospheres. They show a higher sphere forming rate as the first degree or primary spheres, which means that passaging enables a purer cultivation of mammary cells with stem cell properties [30].

Similarly to secondary spheres it was observed that a higher proportion of cells from tumour cell lines form tumourspheres in comparison to those from normal breast tissue [31]. This goes with the assumption of a defect in the self-renewal process caused by a mutation and would be a good simulation for the uncontrolled division of tumour cells.

1.4 Approaches to Determine the Sphere Forming Rate

1.4.1 Counting Mammospheres

The simplest method is directly based on the aforementioned mammosphere assay since the total number of mammospheres at the end of the experiment is counted manually and divided by the number of cells at the experiment start [49]. As the breast cells are very small, it is not possible to determine the actual number of breast cells at the experiment start. Therefore, the total number of breast cells is known approximately only. The result achieved by this approximative method is a hint on the actual sphere forming rate only and very imprecise.

1.4.2 Limiting Dilution Analysis

To determine the sphere forming rate of specific breast (cancer) cells the Limiting Dilution Analysis (LDA) is used, first introduced by Rota et al. in the context of mammospheres [49]. In general, Limiting Dilution Analysis is an approach to quantify the biological activity of cells in a population [35]. Here, one wants to know the proportion of breast cells that forms mammospheres, which leads to a frequency characteristic for the particular cell line under certain conditions.

To conduct the Limiting Dilution Analysis experiment a suspension containing breast cells is plated over a, e.g., 96 well plate, each column containing a different, descending cell density D reached by dilution, which can be expressed as cells per well, cells per cm^2, or cells per ml (see Figure 4a) [38]. The first column comprises the highest density, so that most wells contain mammospheres, while the last column with the lowest density shows as good as no spheres after approximately seven days [49].

After sphere growing, the single wells have to be scored positive or negative for the presence or absence of at least one mammosphere, respectively. Assuming a Poisson distribution within the particular columns of the 96 well plate, the natural logarithm of the fraction of negative wells is plotted against the cell density. The experiment supplies the single dots exemplary shown in Figure 4b. On the basis of this dots a linear regression line is computed. For a detailed description of the derivation of the linear relation see Section 2.2.6. The absolute value of the slope of the linear regeression line represents the sphere forming rate so that one divided by the slope represents the sphere forming proportion.

The Limiting Dilution Analysis, as described previously, comprises several drawbacks. Due to the manual dilution process, it is not guaranteed that each well of an equal dilution contains the same number of cells. This evokes imprecisions since the calculations are based on the assumption that all dilutions in the wells of the same column have exactly the same cell density. The experimental set-up would not fit to the statistical model. Especially at columns with lower densities it is very important that the cell density is equal for each well. If the dilution contains only a few cells, it might be possible that by chance most of the cells are put into one well while the other wells do not contain any cells at all. If the sphere forming rate is high, most of the cells in that single well would form spheres. At the same time the other wells show no spheres indicating a low sphere forming rate since the presence or absence of spheres is assessed only.

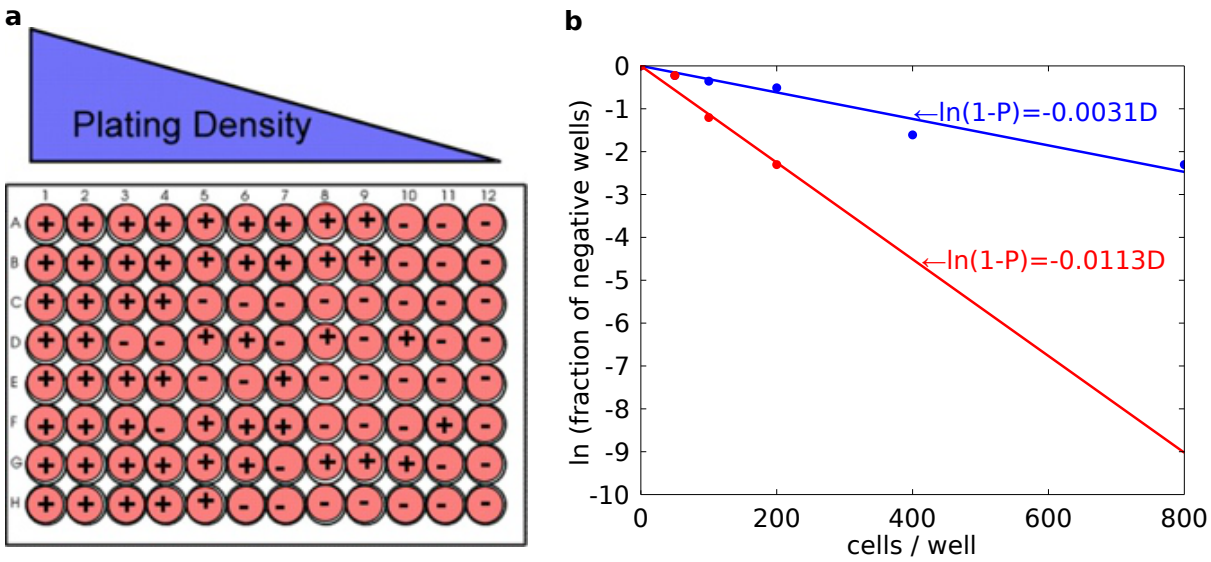

Figure 4: Simplified experimental set-up and synthetic result of two Limiting Dilution Analyses. a) A 96 well plate containing dilutions of breast cells with descending densities equal for each column. "+" means that the well contains at least one sphere, while "-" indicates the absence of mammospheres. Image taken from [49]. b) Limiting Dilution Analysis-plot of synthetic data. The natural logarithm of the fraction of negative wells is plotted against the cell density at the experiment start measured in cells per well. The dots represent the values based on the manual counted information. Each line corresponds to the linear regression line estimated from the dots of the same colour. Assuming these lines belong to two different cell lines, the one corresponding to the red line would have a higher sphere forming rate (0.0113) than the one corresponding to the red line (0.0031). This would mean for the data represented in red that one of about 88 cells forms a sphere, while one of about 323 cells forms a sphere for the data represented in blue.

1.4.3 Live Cell Microscopy

One approach to solve the raised issues is live cell imaging. With this method it is possible to determine the exact number of cells and spheres at a particular time point. This enables the computation of the sphere forming rate without the need of different dilutions by dividing the number of mammospheres at the experiment end by the number of breast cells at the experiment start similar as described in Section 1.4.1. While the manual evaluation of the Limiting Dilution Analysis results in one rate for the whole 96 well plate, calculating the sphere forming rates based on live cell microscopy obtains one rate per well and therefore in a high-throughput manner. If the wells contain the same cell line, the median rate characteristic for this cell line can be computed to sustain a more general value. It is also possible to use a single plate for different cell lines and/or growing conditions. Thus, several experiments are conducted using only one well plate. Also, it is unclear if different cell densities influence the sphere forming rate, by using the same dilution for each condition and cell line the results would be much more comparable without any influence of the cell density.

To realize live cell imaging, images of the well plate are taken. If they are taken for a long period of time at constant time intervals, the result is called a long term time-lapse movie. To compute the sphere forming rate, only images at the beginning and end are

needed. Live cell imaging has already successfully been applied in the context of other cell types like hematopoetic stem cells [50]. Typical applications of live cell microscopy often apply fluorescent markers [32]. However, the general technique also allows for imaging of unstained cells in bright field.

In addition, it might be informative to learn something about the spheres' morphology including cell or sphere size as well as shape or other quantitative features. This can be analysed also by using live cell microscopy.

1.5 Image Processing Frameworks

The huge amount of data produced by live cell microscopy necessitates an automatic analysis. In recent years, several tools for automatic high-throughput image analysis were developed. Commercially available solutions like MetaXpress and Imaris offer powerful options for image processing, but mostly they are very expensive [29, 9]. Often it is not possible to customise commercial programs, which is another disadvantage as most programs have to be heavily adjusted to produce satisfying results on different experimental setups. An open-source alternative is Fiji/ImageJ [4]. Despite its powerful and easy to use macro language and wealth of available image processing algorithms, its disadvantage is the missing modular pipeline system and the not very intuitive user interface. This makes the usage difficult for biologists mostly inexperienced in programming.

Another open-source program is CellProfiler [14, 37]. In contrast to Fiji/ImageJ, CellProfiler provides a lot of modules separated by categories, which can be combined to variable pipelines. To make it easy to use also for users that have no background in image processing, CellProfiler provides elaborated module descriptions particularly for each parameter that can be set within the modules. Furthermore, it is easy to extend CellProfiler by implementing new modules or plugins. Hence, the CellProfiler community has grown quite large, covering users from the biological as well as the computational field. This becomes exceedingly apparent by a view on the number of their citations - 601 citations since 2006, as at January 2013 and by having a look into CellProfiler's active forum [16, 18].

Originally CellProfiler was developed to analyse fluorescent images [14]. Using bright field images bears several advantages in comparison to fluorescent images. For bright field images no fluorescent or other dye that could influence the cells' behaviour and life time is needed. Depending on the type of the fluorescent dye and the cell type it might be not possible to stain the entire cell so that no information about the cell's shape or other features is obtained. Furthermore, it might happen that some cells are not able to become stained by the used dyes, which would lead to unrecognised cells and therefore biased data. In addition, the number of fluorescent dyes is limited. So it would not make sense to waste one channel for cell identification limiting the number of channels used to mark special proteins, RNA, or other cell contents suggesting something about the cell's state [12].

1.6 Aim of this Thesis

In this thesis, we develop a method based on live cell microscopy in combination with image processing to automate the calculation of the sphere forming rate based on the

mammosphere assay. To analyse the huge amount of data produced by live cell microscopy, a fully automated pipeline is created using CellProfiler as a framework. Since we are working on bright field images, a new CellProfiler module for segmentation is created. The application of this pipeline results in the total number of breast cells and mammospheres, which enables the calculation of sphere forming rates for two different cell types. Thus, we exemplary prove the applicability of our approach for assessing the sphere forming rate of single breast stem cells and evaluate the feasibility of CellProfiler as a framework.

Section 2 gives detailed information about general image processing and statistical methods as well as the conduction of the used experiments in this thesis.

The following main part gives details about the mammosphere quantification pipeline i.e. its development, implementation, application, and validation (Section 3.1). The full pipeline is applied to an experiment comprising 18 wells, equivalent to 216 images both for the beginning and the ending taking around 24 minutes and around 36 minutes, respectively. Two different cell lines forming primary spheres are analysed. The manual validation of our method (see Section 3.1.4) yields a f-measure of 0.83 for applying the pipeline to the images of the experiment start and 0.89 for applying the pipeline to the images of the experiment end. Therefore, the number of cells and mammospheres is counted manually, which enables the calculation of sphere forming rates as well. In addition, the results of the application are depicted, compared to the standard methods, and discussed (Section 3.2). We show that the principle idea for the way of automation is correct by comparing the computed rates based on manually counted numbers for two different tumour cell lines with the knowledge of the different aggressiveness of these cells. The feasibility of CellProfiler as a framework is discussed in Section 3.3.

Ideas for further development steps to improve the calculation of the sphere forming rates based on the fully automatic method are proposed in Section 4.

2 Methodological Background

2.1 Image Processing

2.1.1 Mathematical Morphology

The top-hat filter is a well-known technique in the field of mathematical morphology, a sub-category of image processing. An input image gets subtracted by the morphological opening of itself [19]. Morphological opening is the combination of erosion and dilation, which both are basic operators of mathematical morphology originally developed for binary images [44]. Though we are dealing with gray-scale images, we firstly explain the general idea behind erosion and dilation by introducing the processes for binary images.

An erosion shrinks the objects in an image while a dilation shrinks the background and thus the objects are dilated. Figure 5aii and bii are examples for objects represented by the black pixels. Let X be the set of black pixels in an image representing the objects and X^C the set of white pixels representing the background.

The term mathematical morphology originates from using a shape like a circle or rectangle as a mask for the image transformation [44]. The shape or structural element is illustrated by black pixels for erosion and white pixels for dilation, the same colors as the pixels they are applied to (see Figure 5). The set of pixels belonging to the structural element for erosion are represented by B^1 and the pixels belonging to the structural element for dilation by B^2.

For erosion the structural element is shifted to each pixel p belonging to the objects, here represented in black. If all pixels of the image covered by the mask are black as well, the pixel p in the centre stays black. At least one white pixel covered by the mask B^1 leads to turn the pixel white and therefore to an eroded object. The following equation defines erosion in mathematical terms:

$$X \ominus B^1 = \{p | B^1_p \subset X\} \tag{1}$$

The dilation process works analogously except for the pixel colours. Here the structural element is shifted to each white pixel p, belonging to the background, and the pixel p turns black if one or more pixels covered by the mask B^2 are black.

$$X \oplus B^2 = \{p | B^2_p \subset X^C\} \tag{2}$$

In contrast to binary images, gray-scale images do not only have black and white pixels. Therefore, the erosion and dilation are defined over minimum and maximum intensities, respectively [53]. The easiest way is the use of a flat structural element $B : D \subset \mathbb{Z}^2 \longrightarrow S$ with $S = \{0, 1, ..., 255\}$ assuming eight bit images. "Flat" means that the structural element itself has no different intensity levels and therefore it holds that $\forall (s,t) \in D : B(s,t) = 0$. If this is not the case, the value of the particular pixel $(s,t) \in D$ is subtracted or added for computing the minimum or maximum, respectively (see Equation 3 and Equation 4). The structural element B for an image $I : C \subset \mathbb{Z}^2 \longrightarrow S$ is shifted over each pixel $(x,y) \in C$ since it is not possible only to decide between black and white due to the 256 different intensities as common for gray-scale images. Now the intensities of

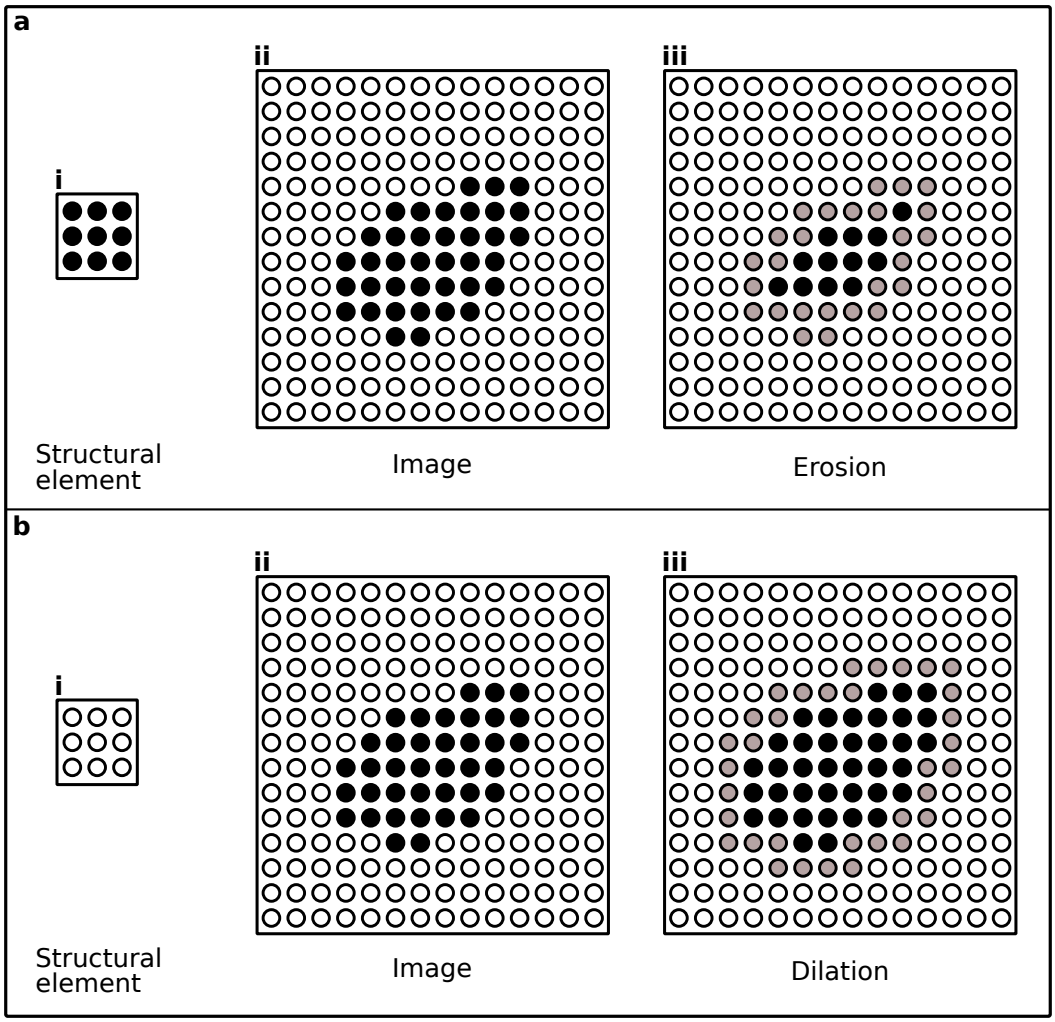

Figure 5: The two parts of morphological opening: a) Erosion: The structural element shown in i is used for erosion. It consists of black pixels solely since it should be applied to the black pixels of the image shown in ii. The central pixel of the structural element is moved on each black pixel p in the image. If all pixels comprehended by the structural element are also black, pixel p will stay black in the eroded image. If at least one pixel in the mask defined by the structural element is white, pixel p turns white. The pixels turned white are illustrated gray in the eroded image shown in iii. They do not belong to the eroded object. b) Dilation: In comparison to the structural element for erosion the structural element for dilation is comprised of white pixels (i) because it should be applied to the white pixels of the image shown in ii. Here the structural element is moved over each white pixel. The pixel becomes black if at least one of the pixels covered by the structural element is black. The pixels turned black are illustrated gray in the dilated image (iii) and belong to the dilated object. Image adapted from [44].

all pixels of the image I covered by the mask B are compared to each other. For erosion the pixel $(x, y) \in C$ covered by the centre of the structural element B gets the intensity equal to the minimum intensity of all pixels covered by the mask B. In contrast within dilation the pixel $(x, y) \in C$ covered by the centre gets the maximum intensity of the pixels covered by the mask B.

In the context of gray-scale images the mathematical definitions of erosion and dilation

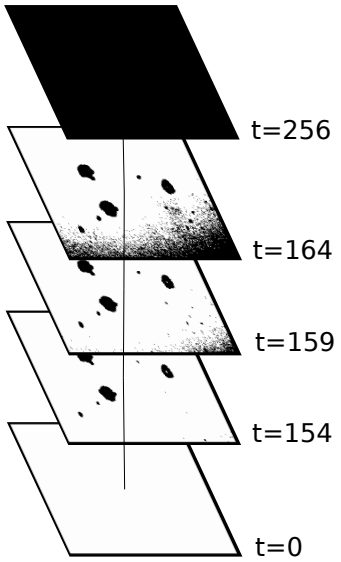

Figure 6: The different threshold levels t used during the MSER algorithm and the resulting binary images. All pixels with an intensity higher or equal to the threshold t are coloured white, while those pixels with a lower intensity are black. Assuming $\Delta = 5$ and $t = 159$ the images for a threshold between 154 and 164 are considered. Each speckle of black pixels forms an extremal region if it is consistent over all of the eleven images for thresholds $154 \leq t \leq 164$.

of an image I are as follows:

$$\forall (x,y) \in C : (I \ominus B)(x,y) = \min_{\forall (s,t) \in D} \{I(x+s, y+t) - B(s,t)\} \tag{3}$$

$$\forall (x,y) \in C : (I \oplus B)(x,y) = \max_{\forall (s,t) \in D} \{I(x+s, y+t) + B(s,t)\} \tag{4}$$

Finally, an opening is an erosion followed by a dilation. When the result is subtracted from the input image, the entire process is called top-hat filter [44]. The applied structural element is a circle. Hence, the method is called "top-hat". White and black top-hat filters exist, enhancing white or black speckles, respectively.

2.1.2 Maximally Stable Extremal Regions (MSER)

In contrast to common thresholding algorithms like Otsu's method [45] the algorithm to detect MSERs does not choose one single threshold and uses this for the whole image or a part of it, but takes every possible threshold between zero and 256 in case of eight-bit images and checks for extremal regions. Extremal regions are defined as a subset of pixels out of the image where the pixels are adjacency within the region and all pixels belonging to the region are either darker or brighter than the pixels around that region. The pixels around a region, referred to as region boundary, are not part of the region themselves but have at least one adjacent pixel belonging to the region.

Starting with a white image and a threshold being zero, the threshold is increased, so that all pixels with an intensity lower than the threshold are visible as black spots on the white background. These black spots are maximum intensity regions. In the end, when the highest threshold of 256 is achieved, the image is completely black since there are

no pixels with a higher or equal intensity as 256. Inverting the intensities and doing the same leads to minimum intensity regions. Figure 6 shows simplified all these 256 images stacked on each other. Each stage represents the extremal regions for one threshold. Now we are searching for the maximally stable extremal regions, which can be determined by examining a set of images following each other in the stack. The size of this set depends on the parameter Δ, which therefore is a measure for the stability of the resulting extremal regions. If we choose the image at threshold $t = 159$ and $\Delta = 5$ the set contains the images between the thresholds $t = 154$ and $t = 164$ (see Figure 6). Now every region that exists in each of the images included in the set defined by Δ is called maximally stable extremal region (MSER).

To describe a region, an extremal region, and the region boundary in a more mathematically way, the following definitions are necessary [40]:

- An **image** I is defined as $I : C \subset \mathbb{Z}^2 \longrightarrow S$ with $S = \{0, 1, ..., 255\}$ representing the pixel intensities of eight-bit images.
- An adjacency neighbourhood relation $A \in C \times C$ is defined. The pixels $p, q \in C$ are adjacent neighbours (pAq) if
$$\sum_{i=1}^{d} |p_i - q_i| \leq 1 \tag{5}$$
where d is the number of dimensions. Here, $d = 2$ because $C \in \mathbb{Z}^2$.
- A **region** R is a continuous subset of C.
- The **region boundary** B is defined as
$$B = \{q \in C \setminus R : \exists p \in R : qAp\} \tag{6}$$
- With this definitions an **extremal region** is $R \in C$ so that
$$\forall p \in R, q \in B : I(p) > I(q) \tag{7}$$
- Figure 6 shows that the regions overlap in the images for the different thresholds. This is called nested extremal regions. Let $R_1, ...R_{i-1}, R_i, ...$ be a sequence of nested extremal regions with $R_{i-1} \in R_i$ and $\Delta \in S$. If $q(i)$ has a local minimum at i, the extremal region R_i is **maximally stable (MSER)** with
$$q(i) = \frac{|R_{i+\Delta} \setminus R_{i-\Delta}|}{|R_i|} \tag{8}$$

2.1.3 Form-Factor

The form-factor f is defined as
$$f = \frac{4\pi a}{p^2} \tag{9}$$
where a is the area and p the perimeter of the object [24]. The object's area a is defined as the number of pixels belonging to the object and the perimeter p is the total number of pixels around the object's boundary. Therefore, completely round objects have a form-factor of one.

2.2 Statistics

2.2.1 Confusion Matrix

A confusion matrix consists of information of actual and predicted classifications. In the case of two classes it is "positive" or "negative". The actual and the predicted values are compared. Therefore, each cell of the matrix (see Table 1) is classified as follows:

- True positive (TP): The actual value of the class is positive and it is correctly predicted as positive.
- False positive (FP): The actual value of the class is positive and it is falsely predicted as negative.
- True Negative (TN): The actual value of the class is negative and it is correctly predicted as negative.
- False Negative (FN): The actual value of the class is negative and it is falsely predicted as positive.

		predicted	
		positive	negative
actual	positive	TP	FN
	negative	FP	TN

Table 1: Confusion matrix comparing the actual and predicted values. This results in the numbers of true positives (TP), false positives (FP), true negatives (TN), and false negatives (FN).

2.2.2 Precision

The ratio between the number of correctly predicted positives and the number of positive predicted is given by the precision defined as

$$precision = \frac{TP}{TP + FP} \tag{10}$$

The rate falls in a range of [0,1] with the best score being one.

2.2.3 Recall

The proportion of correctly predicted positives in the total number of positives is given by the recall. Its definition is as follows:

$$recall = \frac{TP}{TP + FN} \tag{11}$$

The values of the recall are within the interval [0,1]. Again one is the best score.

2.2.4 F-Measure

A combination of precision and recall is the f-measure. It is similar to the average of the two statistical values. Therefore, the f-measure is defined as

$$\text{f-measure} = 2 \cdot \frac{precision \cdot recall}{precision + recall} \tag{12}$$

$$= \frac{2 \cdot TP}{(TP + FP) + (TP + FN)} \tag{13}$$

The range of the values is again given by [0,1] with the best score being one.

2.2.5 Median Absolute Deviation (MAD)

The median absolute deviation (MAD) describes the median of the deviation of the actual values from the median computed for these values [42]. The MDA for a sample with a median X_m is defined by

$$MAD = median(|X_i - X_m|) \tag{14}$$

This measurement is comparable with the standard deviation that refers to the mean value.

2.2.6 Limiting Dilution Analysis (LDA)

As described in Section 1.4 the Limiting Dilution Analysis is performed to determine the sphere forming rate of breast (cancer) cell lines. Dilutions of breast cells are e.g. plated over a 96 well plate with descending densities equal for each column.

After five to seven days each well is scored as positive or negative for the presence or absence of mammopsheres. Therefore, each well complies with a Bernoulli experiment. The Limiting Dilution Analysis assumes that the variation within the wells, for which the same density D is assumed, follows a Poisson distribution if a single cell forms a sphere independently [54]. Let r be the rate of sphere forming, so that rD gives the total number of spheres in a well. This leads to the general density function of the Poisson distribution:

$$P(X = k) = \frac{(rD)^k}{k!} e^{-rD} \tag{15}$$

where X is the random variable and complies with the actual number of mammosphere forming cells and $k \in \mathbb{N}_0$.

The possibility that there is no sphere forming cell complies with $P(X = 0)$ and therefore

$$P(X = 0) = e^{-rD} \tag{16}$$

We are interested in the probability that there is at least one sphere per well according to

$$P(X > 0) = 1 - P(X = 0) = 1 - e^{-rD} \tag{17}$$

By logarithmic calculus this equation can be linearised as

$$ln(1 - P) = -rD \tag{18}$$

with $P = P(X > 0)$. The negative slope of the linear equation is the sphere forming rate r [35].

After determining positive and negative wells, the natural logarithm of the fraction of negative wells i.e. $1 - P$ for each density can be computed. The emerging dots are charted in a plot showing the natural logarithm of the fraction for wells negative against the cell density (see Figure 4b). The absolute value of the slope of the linear regression line that is calculated for the dots and passes the origin represents the sphere forming rate r and $1/r$ represents the sphere forming proportion.

2.3 Conduction of Experiments

All biological data described in this section is produced in collaboration with Dr. Scheel's group at the Institute of Stem Cell Research of Helmholtz Centre Munich.

Both the Limiting Dilution Analyses and the live cell microscopy experiment were conducted for two different cancer cell lines, MDA-MB-231 and MCF7-Ras. MDA-MB-231 is a mesenchymal cancer cell line and therefore more aggressive as epithelial cancer cell lines like MCF7-Ras (see Section 1.1). MDA-MB-231 is originally taken from a Caucasian 51 year old woman [8]. MCF7-Ras originates from the MCF7 cancer cell line from a Caucasian 69 year old woman [7]. After inducing v-Ha-ras, a gene coding a protein involved in the regulation of cell division, the cell line is referred to as MCF7-Ras [47, 39].

2.3.1 Limiting Dilution Analysis

Five Limiting Dilution Analyses to determine the sphere forming rates are conducted. This involves three experiments for MCF7-Ras and two for MDA-MB-231. For every experiment six different dilutions are plated on a 96 well plate. Ten wells are used for each dilution with the highest cell density being thirty cells per well. The concentration is halved for the next adjacent column of wells until the smallest concentration of 0.8 cells per well is achieved. After five days each well is scored for the presence or absence of at least one mammosphere.

The plots of the natural logarithm of the fraction of negative wells against the cell density are created as described in Section 2.2.6. The plots for the five Limiting Dilution Analyses and the particular sphere forming rates are shown in Figure 13. Additionally, the mean and standard deviation of the computed sphere forming rates by the manual Limiting Dilution Analyses distinguished between the cell lines are shown in Table 4.

2.3.2 Live Cell Microscopy

To create the live cell microscopy images in order to compute the sphere forming rate, the cells have to be released from the plate where they are growing adherently. This is done by trypsinization. The non-adherent cells are placed into the mammosphere-medium in

a concentration of 1000 cells per ml. The suspension is filled into an uncoated 96 well plate from ibidi with 100 μl per well. After 24 hours the cells are stabilised in one layer. A total of 18 wells is imaged in time intervals of 30 minutes for five days using a cell observer microscope (Zeiss). Due to the limited camera resolution, every well is divided into overlapping tiles (i.e. fields of view) (see Figure 9a). Images are taken in a space of time of four days and 22 hours i.e. for 237 time points, which makes a total number of 51.192 images, producing a total storage of about 50 GB.

3 Mammosphere Quantification Pipeline and Calculation of the Sphere Forming Rate

3.1 Pipeline Development, Implementation, Application and Validation

3.1.1 Development

To analyse the huge amount of images produced during live cell microscopy automatically, several image processing steps are needed that perform robustly on the full dataset without user interaction. Hence, the following subsections describe challenges and the necessary used operations to identify breast cells and mammospheres in bright field images. For details about the used algorithms please refer to Section 2.

Challenges

Most algorithms implemented in CellProfiler are parametrized to perform well on fluorescent images. It would be preferable to be able to use existing algorithms, which have the only constraint that objects are brighter as the background as common in fluorescent images.

A major difficulty in image processing is the uneven illumination of images due to unbalanced lightning or not completely translucent medium. This refers to single images as well as the entire well. Especially the centre of the well is ablazed with light so that there are large discrepancies at different positions in the same well (see Figure 9a). The center of the well is brighter while the outer area is darker. Therefore, a background correction is necessary to achieve acceptable results in the identification of breast cells and mammospheres. Another problem, particularly in the context of bright field images, is the heterogeneous intensity of the objects. This is observable in Figure 3 as the single cell on the left side shows a dark frame and a bright interior. Furthermore, an uneven intensity distribution is depicted in the right picture of Figure 3 for the mammosphere. In this case the objects are both darker and brighter as the background, which renders the distinction between the objects and the background difficultly.

In addition, debris and air inclusions hamper the correct identification of cells and mammospheres. Debris might be identified as objects by mistake while large air inclusions create huge, black speckles whereby cells and mammospheres in the same area are not visible. Air inclusions are also reliable for falsely identified objects since they are heterogeneously illuminated as well as the objects themselves.

To identify objects, a binary image deciding between fore- and background and therefore serving as a mask is necessary. To create this binary image, which is called segmentation, different methods with different complexity exist. One of the most widely used approaches is thresholding based segmentation. An intensity threshold that decides whether a pixel with an intensity above the threshold is turned white and a pixel with an intensity lower or equal to the threshold is turned black is determined. Common thresholding algorithms, e.g. the algorithm developed by Otsu, determine an intensity threshold for the whole image (global) or parts of it (adaptive) [45]. Since Otsu's method assumes a bimodal

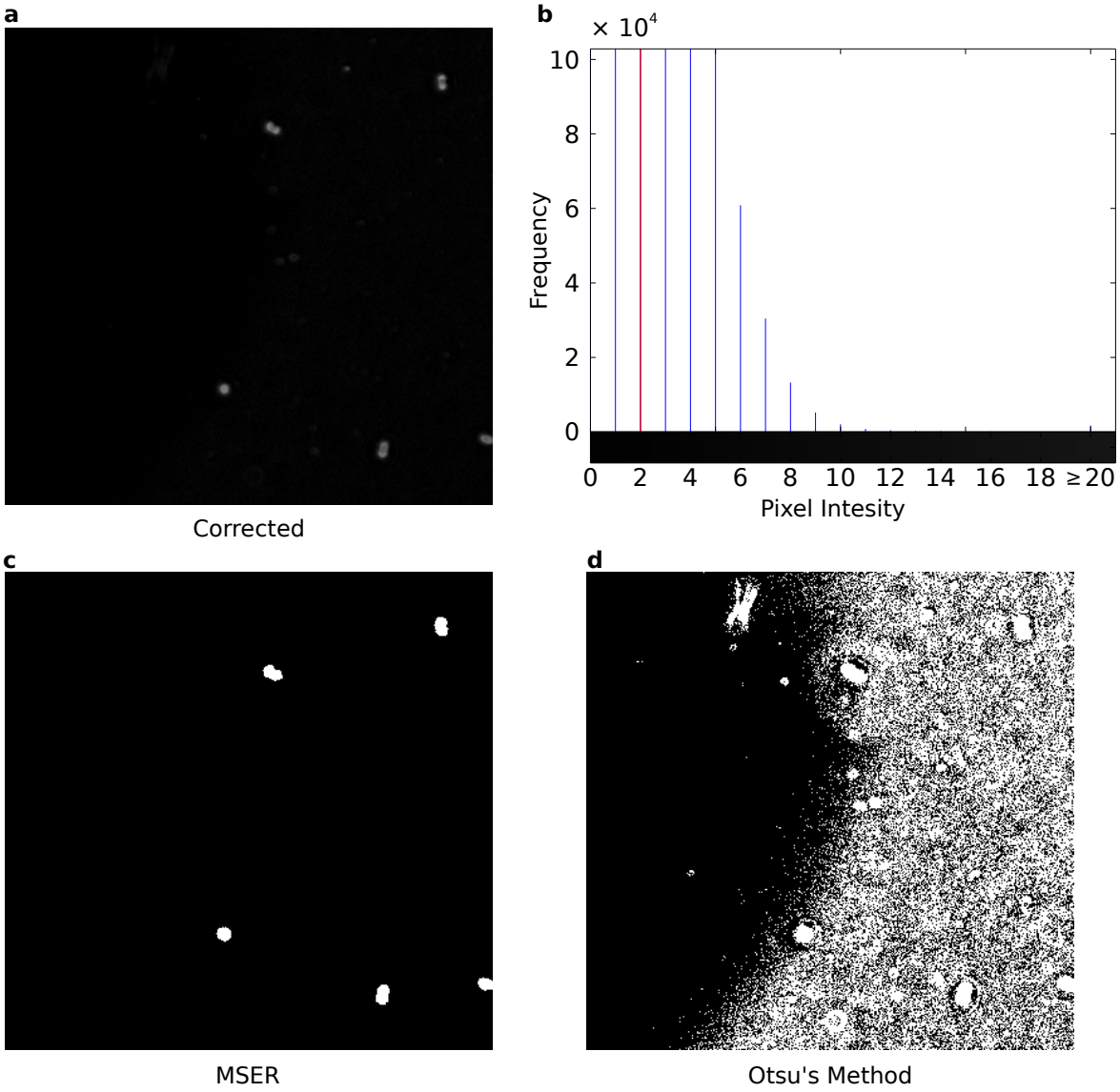

Figure 7: Comparison of different segmentation algorithms. a) Background correction of an inverted bright field image using a white top-hat filter. b) Histogram of pixel intensities. The red vertical line marks the threshold selected by Otsu's algorithm (threshold: 2). Since there are only a few pixels with a high intensity (summed up at an intensity of 20), it is not possible to decide between back- and foreground by one simple threshold (d). c) Segmentation by the MSER algorithm, which performs more robust because each possible threshold level is considered. The displayed images are only excerpts while the pixel intensity histogram is based on the entire background corrected image. The segmentations are also calculated on the entire images.

intensity distribution to determine the threshold, the approach collapses for some images especially bright field images e.g. if they comprise a lot of dark pixels and only a few bright pixels (see Figure 7).

Single Steps

To use existing CellProfiler modules specialized on fluorescent images, the raw bright field

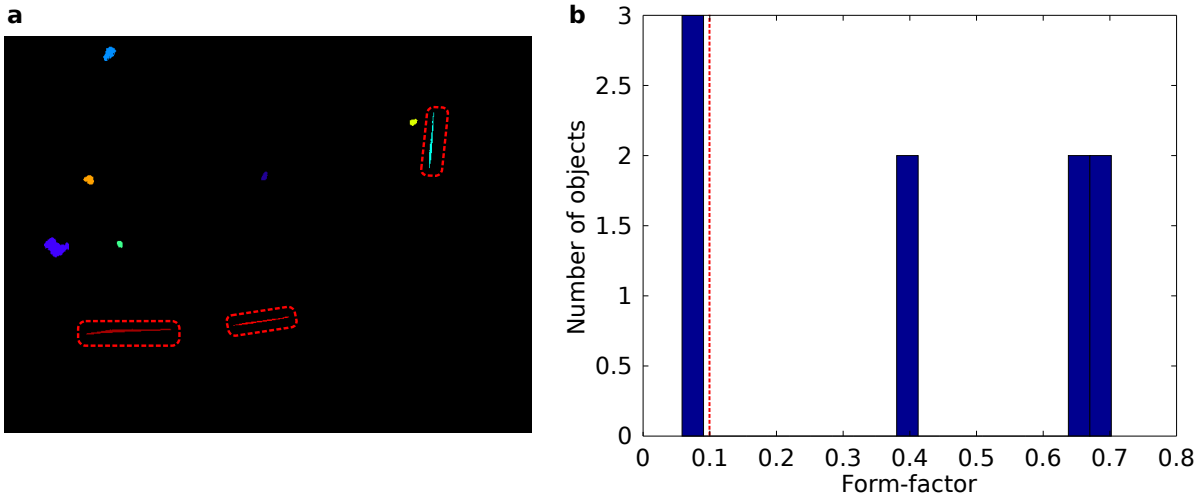

Figure 8: Filtering based on morphological quantification. a) Identified objects in an image of the below right corner of the well after background correction and segmentation. The three objects marked by a rectangle are falsely identified caused by a erroneously enhanced white line at the well's border. This three objects have a form-factor less than 0.1 as depicted in the histogram of the number of objects and their form-factor (b). The other objects have higher form-factors, which enables deciding between falsely identified objects and true objects by their form-factor.

images are inverted so that the objects appear brighter as the the background.

To correct for uneven illumination, in a first step the image is smoothed by an opening resulting in an estimation of the background. Afterwards the background is subtracted from the original image resulting in a flattened image where all objects should be evenly illuminated (see Figure 9iii). The whole process is referred to as top-hat filtering [19].

After inversion and background correction a segmentation is conducted (see Figure 9iv). A method especially suitable for bright-field images is the MSER (**M**aximally **S**table **E**xtremal **R**egions) algorithm (see Figure 7c), which was originally developed to detect correspondences in two images taken from different viewpoints but was already successfully applied for cell detection [40, 6]. Its superior performance on comparable time-lapse experiments in comparison to Otsu's method has recently been shown by Buggenthin et al. [12]. Its advantage is the usage of all threshold levels instead of restriction to one single threshold for the whole image or at least parts of it. For further information on the MSER algorithm's strategy see Section 2.1.2.

The final aim in the pipeline is the identification of the breast cells and mammospheres, referred to as objects, in the images. The pixels of the input image are assigned to several objects depending on the corresponding binary image achieved by segmentation.

In spite of the background correction and the following segmentation, some of the objects are erroneously identified (see Figure 9iv and Figure 8a). With the previous object identification it is possible to measure morphological information like the size or mean pixel intensity of the particular objects. If morphological traits characteristic for falsely identified objects exist, it is possible to eliminate the falsely identified objects by filtering by these traits. An example i.e. filtering by the form-factor (defined in Section 2.1.3) is depicted in Figure 8.

Figure 9 (*following page*): Workflow of the developed method. A 96 well plate is filled with a breast (cancer) cell suspension. a) Due to limited resolution of the microscopic camera each well is subdivided into twelve positions using a grid. For each of the twelve positions per well images are taken in constant time intervals. b) For each image (i) the following steps are processed: After loading the image into CellProfiler it gets inverted (ii). The background correction by a white top-hat filter follows (iii). Further, the corrected image is segmented using the MSER algorithm (iv). Using the segmented image as a mask the objects, i.e. breast cells and mammospheres are identified (v). Some images have bright white lines at the border of the frame surrounding the well. These lines are recognized by the MSER algorithm causing false positive identified objects (see red lines in v). Hence some features, e.g. area and formfactor, are measured for each object (vi) to filter false positive objects (vii). c) Knowing the number of objects for each position and therefore for the entire well it is possible to compute the sphere forming rate.

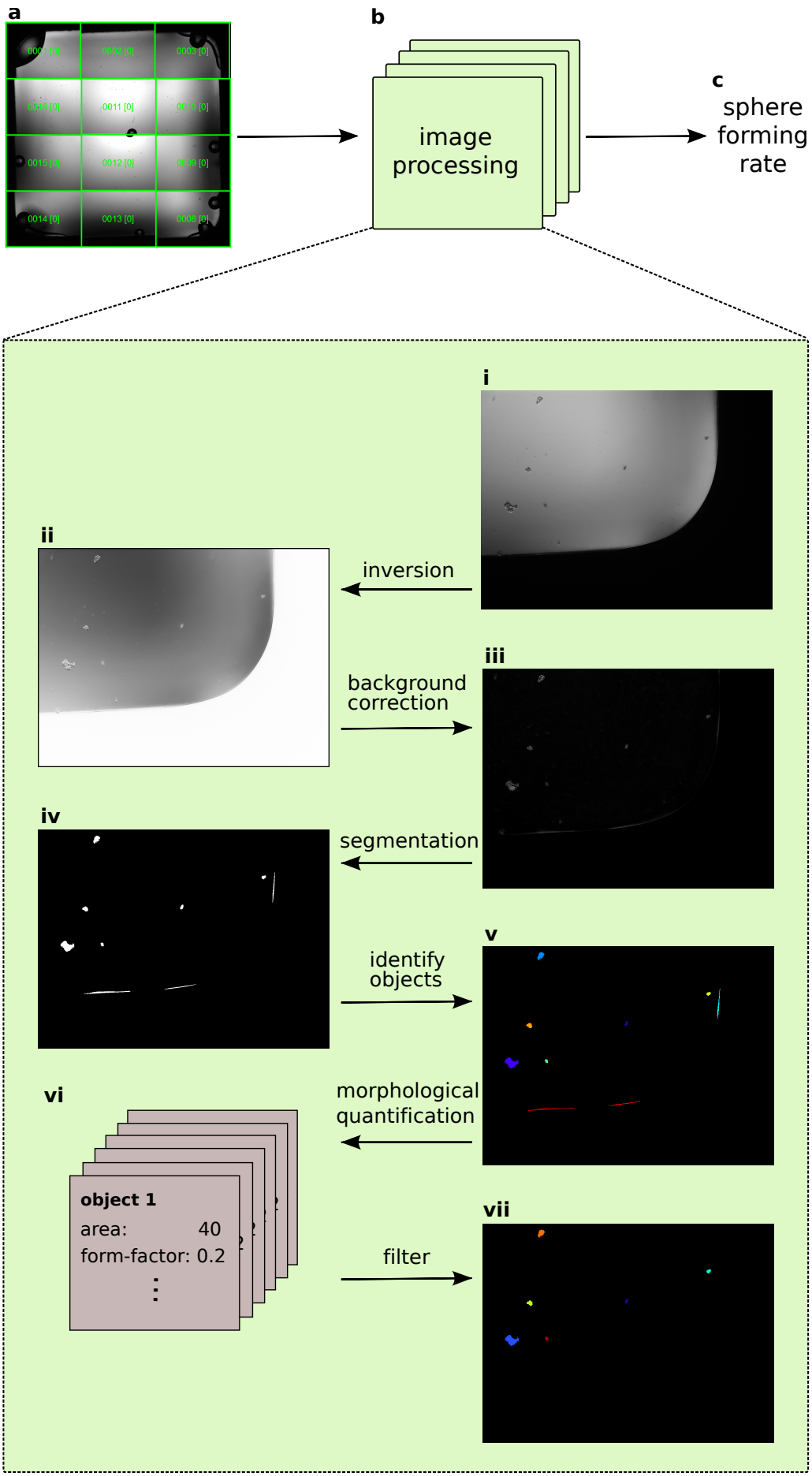
a
b
image processing
c
sphere forming rate
i
ii
inversion
iii
background correction
iv
segmentation
v
identify objects
vi
morphological quantification
object 1
area: 40
form-factor: 0.2
vii
filter

3.1.2 CellProfiler Implementation

As a framework for our pipeline we use CellProfiler providing a module based pipeline system. We incorporate the existing modules as far as possible and create a new module for the bright field segmentation.

CellProfiler is written in object-oriented Python 2.7 depending on several packages and frameworks [37, 3, 17]. In this work we used the following versions:

- Matplotlib 1.3.x for Python 2.7
- WxPython 2.8.12.1
- Java Development Kid (JDK) 1.6.x
- Cython 0.19.1
- MySQLdb 1.2.3
- NumPy 1.7.0 for Python 2.7
- SciPy 0.11.0 for Python 2.7
- Python Imaging Library (PIL) 1.1.7 for Python 2.7
- H5Py 2.0.1 for Python 2.7
- Setuptools 0.6c11 fpr Python 2.7

Installing those dependencies and frameworks is required to achieve a working developer version of CellProfiler. The source code was obtained from [2].

Although CellProfiler is written in Python, it is possible to include C and C++ code using the wrapper framework Cython for a better performance in speed [1]. This is recommended for computationally complex algorithms and therefore used in this work.

CellProfiler's class structure makes developing new modules comfortable since a good explanation of the basic classes and requirements for new modules is provided [26]. Its data structure is divided into two parts, (i) pipeline data and (ii) workspace data. While pipeline data comprises information about the modules and their settings contained in the current pipeline and does not change between the runs, workspace data stores e.g. images or measurements used during processing the pipeline. Each module inherits from the python class *cellprofiler.cpmodule.CPModule*, which provides methods for the module settings displayed in the user interface and methods that are processed while a pipeline is running. The modules used by the current pipeline are managed by *cellprofiler.pipeline*.

As mentioned before, CellProfiler was originally developed to analyse fluorescent images. Therefore, the image is inverted firstly using Cellprofiler's *ImageMath* module with the "Invert" operation after loading the image by the *LoadImages* module [22, 23]. The image is solely inverted without changing the relative intensities (see Figure 9ii).

The background correction is done for the inverted image using the module *EnhanceOrSuppressFeatures* already existing in CellProfiler [19]. Since the cells should be enhanced in comparison to the background, the operation "Enhanced" is selected. The module provides different methodologies for background correction. The used one is dependent on the parameter "Feature type". Here we choose "Speckles" so that a white top-hat filter, a

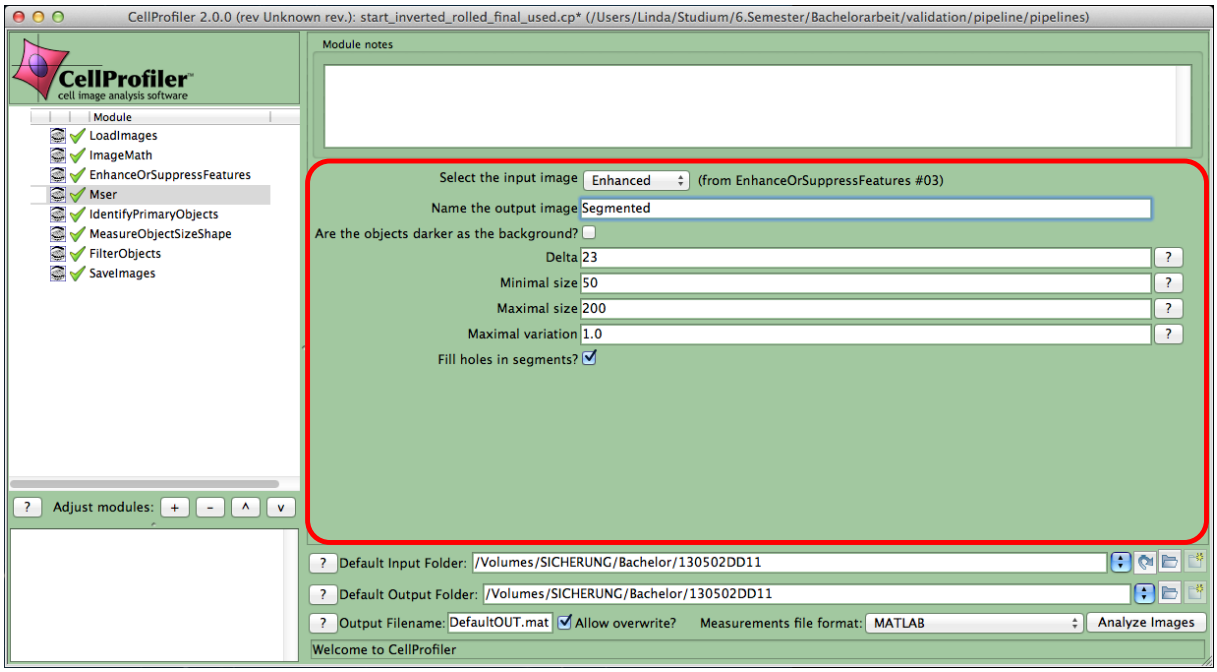

Figure 10: Screenshot of the *Mser* module. The red rectangle marks the *Mser*-specific part of the user interface including its parameter setting. In the left column the modules of the current pipeline are listed and below the red rectangle default paths can be inserted and the output-file for the measurements can be specified.

well-known technique in image processing, is used (for details see Section 2.1.1). "White" top-hat filter means that the white speckles are enhanced. Since the original image is inverted before the background correction, the cells and mammospheres are brighter as the background so that the method works well for our purposes.

The size of the top-hat filter depends on the parameter "Feature size". Therefore, the value of this parameter is smaller for applying the pipeline to the images of the experiment start than for applying it to the images of the experiment end (see Table 2). The larger the structural element, the higher the run time since the intensities of more pixels have to be compared. This explains the longer run time of the pipeline for the images of the experiment end mentioned before.

A large part of this work is the integration of the thresholding algorithm based on determining the MSERs in CellProfiler. Therefore, we create a new CellProfiler module.

A linear time implementation of the MSER algorithm was made by Oliver Hilsenbeck using C++. Since CellProfiler is written in Python, it is necessary to wrap the C++ code for usage in Python [3]. Therefore, Cython is used, which is a compiler for Python and the extended Cython programming language [1]. The Cython programming language is a superset of Python and additionally it is possible to use C/C++ types and functions. The Cython compiler generates a C/C++-extension module, which can be imported by Python.

As the main C++ class uses a deque (i.e. a double ended queue) with a self defined space allocator as class variable, it is not possible to wrap this class directly via Cython. Hence, a C++ wrapper-class is implemented defining a function that calls all necessary methods to conduct the MSER algorithm for one image. This wrapper-class is again wrapped by

Cython to create the C++ extension. So it is possible to instantiate an object of the C++ wrapper-class within CellProfiler's Python code and call its function.

A screenshot of the *Mser* module is shown in Figure 10. The following parameters can be set:

- **Select the input image:** To each image used in the pipeline before a name was assigned. This name can be chosen here.
- **Name the output image:** A name can be chosen to address the resulting image in following modules.
- **Are the objects darker as the background?** Yes / No
- **Delta:** Defines the size of the threshold interval. The higher, the more stable the regions. (see Figure 6)
- **Minimal size:** Minimal size of the MSERs in pixel.
- **Maximal size:** Maximal size of the MSERs in pixel.
- **Maximal variation:** If two regions are nested and their relative variation is below this threshold, only the most stable region is selected [11]. Usually the value is 1.0.
- **Fill holes in segments?:** If the white MSERs have a black hole in their middle, the hole is filled white if selected.

To ensure that the included *Mser* module works correctly, we compare it with the Matlab implementation. Therefore, we apply the MSER algorithm both with the CellProfiler and the Matlab implementation with different parameter settings for a small test set containing ten images. As expected, pixel by pixel comparison shows that the output images are 100 % identical, which proofs the correctness of our integration.

As we want to declare the foreground pixels of the segmentation to objects, the module *IdentifyPrimaryObjects* is used with the inverted image as input and the binary image, resulting from the MSER segmentation, as a mask (see Figure 9v) [21]. During development a bug in the module *IdentifyPrimaryObjects* was detected and reported [28]. As a workaround we correct the error in our local development environment and in the meantime the correction was submitted to the upcoming release by CellProfiler's development team.

CellProfiler's module *MeasureObjectSizeShape* is used to compute several features per object, especially the form-factor [24]. The form-factor enables filtering falsely identified objects with an elongate shape if compared to breast cells or mammospheres, which are more rounded. To determine the threshold where the objects with a lower form-factor are discarded, we made histograms of the form-factor for several images. It is obvious that almost all false objects caused by the well's border have a form-factor less than 0.1 and the other objects have a form-factor higher than 0.1. An exemplary image with its resulting histogram is depicted in Figure 8.

Therefore, the objects with a form-factor less than 0.1 are discarded using the *FilterObjects* module [20]. To illustrate the identified objects and compare the object areas as the result of the pipeline with the original image, we extend the *SaveImages* module so that it is possible to save objects as binary image, where the objects are white and the background

Parameter	experiment start	experiment end
LoadImages		
File type to be loaded	individual images	
Load the input as images or objects?	Images	
Name this loaded image	Image	
Rescale intensities?	No	
Extract metadata from where?	None	
ImageMath		
Operation	Invert	
Name the output image	Inverted	
Select the first image	Image	
Multiply the first image by	1.0	
Raise the power of the result by	1.0	
Multiply the result by	1.0	
Add to the result	0.0	
Set the values less than 0 equal to 0?	No	
Set the values greater than 1 equal to 1?	No	
Ignore the image masks?	No	
EnhanceOrSuppressFeatures		
Select the input image	Inverted	
Name the output image	Enhanced	
Select the operation	Enhance	
Feature type	Speckles	
Feature size	15	30
Mser		
Select the input image	Enhanced	
Name the output image	Segmented	
Are the objects darker as the background?	No	
Delta	23	20
Minimal size	50	250
Maximal size	200	14000
Maximal variation	1	
Fill holes in segments?	Yes	
IdentifyPrimaryObjects		
Select the input image	Inverted	
Name the primary objects to be identified	Spheres	
Typical diameter of objects, in pixel units (Min, Max)	(5, 50)	(10, 200)
Discard objects outside the diameter range?	No	
Try to merge too small objects with nearby lager objects?	Yes	
Discard objects touching the border of the image?	No	
Select the thresholding method	Binary image	
Select the binary image	Segmented	
Method to distinguish clumped objects	None	
Retain outlines of the identified objects?	No	
Fill holes in identified objects?	No	
Handling of objects if excessive number of objects identified	Continue	
MeasureObjectSizeShape		
Select objects to measure	Spheres	
Calculate the Zernike features?	No	
FilterObjects		
Name the output objects	Filtered	
Select the object to filter	Spheres	
Filter using classifier rules or measurements?	Measurements	
Select the filtering method	Limits	
Select the measurement to filter by Category	AreaShape	
Select the measurement to filter by Measurement	FormFactor	
Filter using a minimum measurement value	Yes	
Minimum value	0.1	
Filter using a maximum value	No	
SaveImages		
Select the type of image to save	Objects	
Select the objects to save	Filtered	
Save as grayscale or color image?	Binary	

Table 2: Complete parameter setting of the pipelines separated, if relevant, by experiment start and end. This information suffices for reconstruction in CellProfiler. All parameters not listed here are dependent on the particular working system.

is black [25]. In addition, CellProfiler stores all measurements and information about the pipeline in a MAT-file [43].

3.1.3 Application

The pipeline is applied to one live cell microscopy experiment comprising 18 wells, equally split for the cancer cell line MDA-MB-231 and the cancer cell line MCF7-Ras (see Section 2.3.2). Since analysing dynamics of sphere growth is out of scope of the thesis, only the images of the first and last time points i.e. 432 images are considered

Each of the methods used in the pipeline has plenty of parameters. Determining the best parameter setting is a great challenge since the different parameters influence each other. As a lot of parameters are dependent on the objects' sizes, different parameter settings for determining the number of cells at the experiment start and the number of mammospheres at the end are chosen. Table 2 describes the parameter set for each module used for the pipelines necessary for reconstructing the results and independent from the particular working system.

Applying the pipeline to the experiment with the different parameters yields a run time of about eight seconds per image measured on a 1.8 GHz Intel Core i5 processor with 8 GB RAM running OS X Mountain Lion (10.8.4) storing the images on an external HDD connected via USB 3.0. Full analysis of 2304 images for a whole 96 well plate would take about five hours and twenty minutes.

To compute the sphere forming rate, the total number of cells and mammospheres has to be determined. Therefore, we use the measurement "Count_Filtered" contained in the output MAT-file ("Filtered" is the name of the identified objects after filtering). The number of cells and mammospheres is calculated for each well using Matlab [43]. To compute the sphere forming rate the number of mammospheres at the experiment end is divided by the number of cells at the experiment start. This is done separately for the single wells. For the wells containing the same cell lines and therefore the same conditions the median rate and the appropriate median absolute deviation is computed. We choose the median instead of the mean since it is more robust due to the lower influence by outliers.

Positions including an air inclusion in an area that covers more than about 90 % of the whole image are left out since it is not possible to observe objects (see Figure 11). As the air inclusions grow in the course of time, we factor these positions into the computations determining the number of breast cells at the experiment start and exclude them from the calculation of the number of identified mammospheres at the experiment end.

3.1.4 Manual Validation of the Pipeline Performance

The aim of the pipeline is the correct identification of single cells and mammospheres and the computation of a correct sphere forming rate characteristic for specific cell lines under certain conditions. Therefore, it is important how many objects are identified correctly, how many objects are missed, and how much debris is detected by mistake.

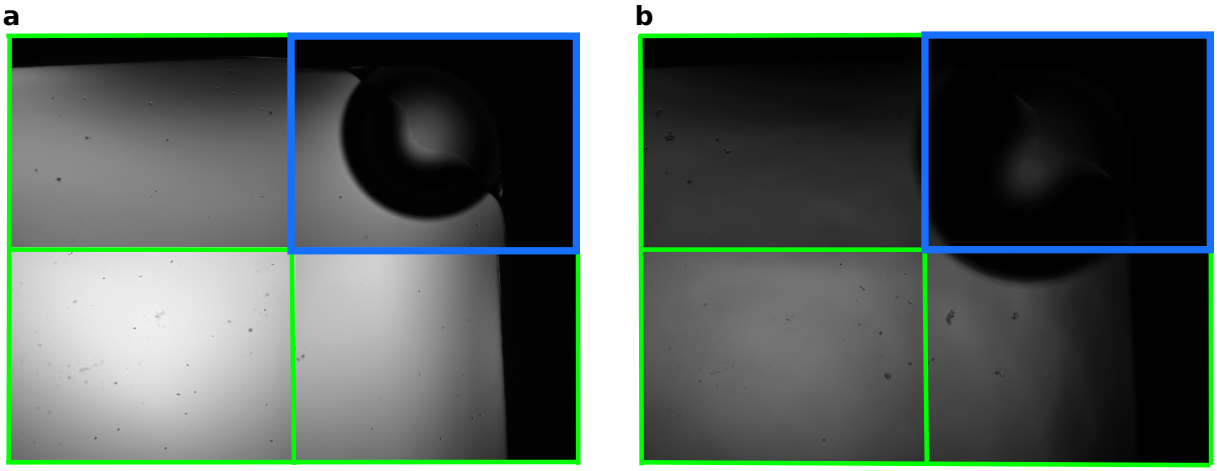

Figure 11: Growing air inclusion. a) Cutout of an entire well consisting of images for four positions covering the right upper corner of the well. The image was taken at the start of the experiment. The upper right, blue-rimmed position comprises a small air inclusion that does not cover the entire image so that it is still possible to observe breast cells. The same cutout is shown in b for the end of the experiment. It is obvious that the air inclusion covers the entire position, it even shades off into the adjacent position. Detecting mammospheres is not possible so that it does not make sense to use the output of the pipeline estimated for this position.

To evaluate the performance of the automatic object identification, we define nine different categories:

- **Correct** - Objects that are at least covered by one segment i.e. identified MSER depicted as white spot in the segmentation image (see Figure 9iv). Each segment is counted once maximally.
- **Missed** - Objects that are not covered by a segment at all.
- **Oversegmented** - Segments that cover objects, which are already covered by another segment counted as "Correct".
- **Undersegmented** - Segments that cover more than one object.
- **Debris** - Segments that cover anything else as objects e.g. dirt or air bubbles.
- **True positives** - Objects that are at least covered by one segment. Oversegmented and undersegmented objects are counted once. (the same as "Correct")
- **False positives** - Everything that is covered by a segment without being an object and all segments that cover an object that is already covered by another segment counted as true positive.
- **True negatives** - This value is always zero since it is not possible to count the region that should not be identified e.g. background.
- **False negatives** - Objects that are not covered by any segment and all objects that are undersegmented except the one that is counted as true positive.

The detailed definitions of true positives, false positives, true negatives and false negatives are given in Section 2.2.1.

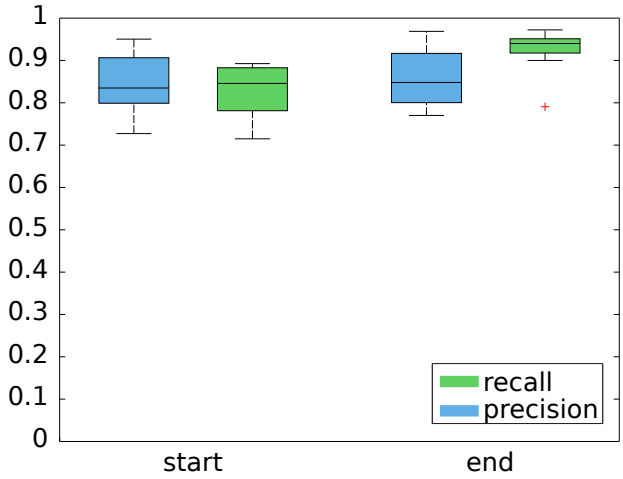

Figure 12: Boxplot of precision and recall divided into the experiment start and end. The values are based on the manual counts as described in Section 3.1.4 for eight wells, four of each cell line. The central mark on the boxes is the median and the lower and upper bound represent the 25 and the 75 percentiles, respectively. The vertical lines under and over the boxes are the whiskers extending to the most extreme data points. Additionally, outliers are marked by a red cross [41].

By superimposing the original image and the binary image resulting from our pipeline, it is possible to manually determine the particular numbers of the single categories. This is done for a total of eight wells, four for each cell line, both for experiment start and end. These values enable the computation of statistical measurements quantifying the accurateness of the method.

One question is, how many of the segments cover objects. The total number of segments and therefore the number that is used to compute the sphere forming rates complies with the sum of true positives and false positives. The rate of how many of these are really cells or mammospheres is given by the precision.

Another question refers to the number of cells that is identified correctly. How many of the actual total number of cells or mammospheres are identified? The actual number of cells is equal to the sum of true positives and false negatives. The rate, which measures this, is the recall.

The average of precision and recall is given by the f-measure. Hence, it is a general measurement for the quality of the entire method (see Section 2.2). The results of the manual counting and the statistical values described before are given in Table 3 and additionally precision and recall are shown in Figure 12.

Given the manual validation, it is obvious that the pipeline performs slightly better on the images of the experiment end than on the images of the experiment start (see Figure 12). Especially the recall determined for the pipeline for experiment end is very high except one outlier (0.791). The decreased performance for the pipeline at experiment start can be explained by the relative huge number of debris (264) and missed cells (301). Since the breast cells do not differ in size if compared to debris, filtering over the objects' sizes is difficult. Furthermore, the images are often badly illuminated close to the well's border, which leads to non-recognized objects.

As proved by this manual validation, our automatic pipeline promises good results in

Experiment time	start	end
Number of manually counted cells/mammospheres	1757	673
Number of automatically counted cells/mammospheres	1728	724
Correct	1456 (82.9 %)	621 (92.3 %)
Missed	301 (17.1 %)	52 (7.7 %)
Oversegmented	8	1
Undersegmented	0	0
Debris	264	102
True positives	1456	621
False positives	272	103
False negatives	301	52
Precision	0.84 ± 0.07	0.86 ± 0.07
Recall	0.83 ± 0.07	0.92 ± 0.06
F-Measure	0.83 ± 0.05	0.89 ± 0.05

Table 3: The performance of our pipelines was manually measured for eight wells, four for each cell line, both for experiment start and experiment end. The number of correct, over- and undersegmented segments was counted as well as the number of segments covering debris and the number of missed objects as defined in Section 3.1.4. Percentages refer to the number of manually counted breast cells and mammospheres. In addition the number of true positives, false positives and false negatives was counted to compute the precision and recall for our methodology. Hereby the f-measure was calculated. Shown are the mean values and the corresponding standard deviations.

determining the number of cells and mammospheres in bright field images. Therefore, it is a auspicious alternative to calculate the sphere forming rate of breast cells.

3.2 Sphere Forming Rate

3.2.1 Determining Sphere Forming Rate

The computation of the sphere forming rate for the two cell lines MDA-MB-231 and MCF7-Ras is done by two different methods: (i) the computation using the manual counts of the live cell microscopy images, and (ii) the computation using the automatically determined numbers by analysing the live cell microscopy images with our pipeline.

Since MDA-MB-231 and MCF7-Ras are mesenchymal and epithelial cancer cell lines, respectively, it is expected that MDA-MB-231 is more aggressive as MCF7-Ras. Therefore, the sphere forming rate of MDA-MB-231 is expected to be higher than the sphere forming rate of MCF7-Ras.

The results based on our automatic and manual method and additionally by Limiting Dilution Analyses conducted by Dr. Scheel's lab are depicted in Table 4 as an overview.

	Method	Sphere forming rate		Required Time	
		MDA-MB-231	MCF7-Ras	Experiment	Analysis
	Limiting Dilution Analysis	0.14 ± 0.08	0.21 ± 0.15	∼2h	∼25 min (counting)
live cell microscopy	manually counted rates	0.40 ± 0.04	0.36 ± 0.02	≥2h	∼20 min (counting)
	automatically counted rates	0.40 ± 0.05	0.38 ± 0.04	≥2h	∼3 min (run time)

Table 4: Mean and standard deviation of the sphere forming rates determined by Limiting Dilution Analysis. The rates determined on the basis of live cell microscopy are depicted as median and the corresponding median absolute deviation. In addition, the required time to obtain one rate for one cell line is depicted separated into the time to conduct the experiment and the time to analyse the number of the cells and mammospheres.

Moreover, the experiment and analysis time required to obtain one rate for one cell line is represented in this table.

The number of cells and mammospheres determined within the manual validation on the basis of eight wells enables computation of a sphere forming rate. The rates and their corresponding standard deviations are 0.40 ± 0.04 and 0.36 ± 0.02 applied to MDA-MB-231 and MCF7-Ras, respectively (see Table 4). This results in a difference of 0.04 between the two cell lines.

The sphere forming rates achieved by the division of the automatically determined number of mammospheres at the end of the experiment by the number of cells at the beginning of the experiment are similar. The median rates applied to MCF7-Ras (0.38) are identical except the higher median absolute deviation (0.04) if determining the rate by the automatic approach. In contrast, the median rate applied to MDA-MB-231 (0.40) is slightly higher (0.02) if determined automatically and the corresponding median absolute deviation (0.05) is higher as well. Due to the higher sphere forming rate computed for MDA-MB-231, the difference between the rates applied to the two cell lines is higher (0.02).

Since MDA-MB-231 is a more aggressive cancer type as MCF7-Ras, the results comply with our expectations insofar as the sphere forming rate established for MDA-MB-231 is by trend higher as the one established for MCF7-Ras. This holds for the manual as well as for the automatic method. Therefore, this result confirms the general approach of dividing the total number of mammospheres at the experiment end by the total number of breast cells at the experiment start. Moreover, the automatically determined values are good enough to compute reasonable sphere forming rates.

3.2.2 Comparison to Other Approaches

Since our method is an alternative to the standard sphere forming assay i.e. its part of computing the sphere forming rate and the Limiting Dilution Analysis, five Limiting

Dilution Analyses are conducted by Dr. Scheel's group to compare the resulting rates with those of the methods based on live cell microscopy (see Section 2.3.1). This involves three experiments for MCF7-Ras and two for MDA-MB-231.

The sphere forming rates determined by the classic Limiting Dilution Analyses are very different within the particular cell lines leading to high standard deviations (0.08 for MDA-MB-231 and 0.15 for MCF7-Ras). So the rates determined for MDA-MB-231 fall in a range of [0.084, 0.203] and those for MCF7-Ras fall in a range of [0.074, 0.374].

We make the assumption that the sphere forming rate is characteristic for certain breast cell lines. Due to the wide ranges of the established rates the results do not comply with this assumption.

There are two possible explanations for the different values within the same cell lines. (i) The breast cancer cell populations used for the Limiting Dilution Analyses are heterogeneous in matters of sphere forming rate. For the experiments only cells of different parts of the populations were taken by accident. (ii) Due to the overall small numbers of cells used for the Limiting Dilution Analysis, small differences of the cell density in the wells that are assumed to contain the same dilution have a big influence on the statistical values.

As described in Section 2.3.2, 100 μl of a dilution with 1000 cells per ml is filled in each well for the live cell microscopy experiment. This would be consistent with 100 cells per well. Counting the breast cells in the images of the experiment start shows that the actual number of cells per well varies between 187 and 261 for the eight manually analysed wells (see Figure 14a, b). This is about twice as much as expected. Even if the total expected number for the particular wells in the Limiting Dilution Analysis is smaller, it is likely that the actual cell numbers differ from the expected numbers as well. The advantage of our approach is the independence on the exact cell density in a well.

Using higher cell densities to compensate the impact of different dilutions of wells which should comprise the same dilution does not make sense since this would cause mammospheres in each well. Even small dilutions like 30 or 15 cells per well lead to a fraction of negative wells of zero as each well contains at least one mammosphere. If the fraction of negative wells is zero, the natural logarithm of the fraction of negative wells is minus infinite, which is not possible to plot in the Limiting Dilution Analysis diagram. This leads to a smaller number of dots used as basis for the calculation of the linear regression line and therefore a less representative rate.

It was expected that MDA-MB-231 is more aggressive as MCF7-Ras. This difference is not detectable in the results of the Limiting Dilution Analyses since the highest rate determined for MCF7-Ras (0.374) is much higher as the highest rate determined for MDA-MB-231 (0.203). Moreover, the smallest rate determined for MCF7-Ras is 0.074 while the smallest rate determined for MDA-MB-231 is 0.084, which means that the range determined for MDA-MB-231 is located within the range estimated for MCF7-Ras. Even the mean values disagree with this expectation as the mean rate applied to MCF7-Ras (0.21) is higher as the mean rate applied to MDA-MB-231 (0.14).

Counting the cells and mammospheres manually using a microscope as tried in the classical sphere forming assay is not an alternative since it is not possible to have the entire well in the field of view through the microscope at the same time. Therefore, it would be necessary to move the well plate, which provokes movement of the cells and therefore

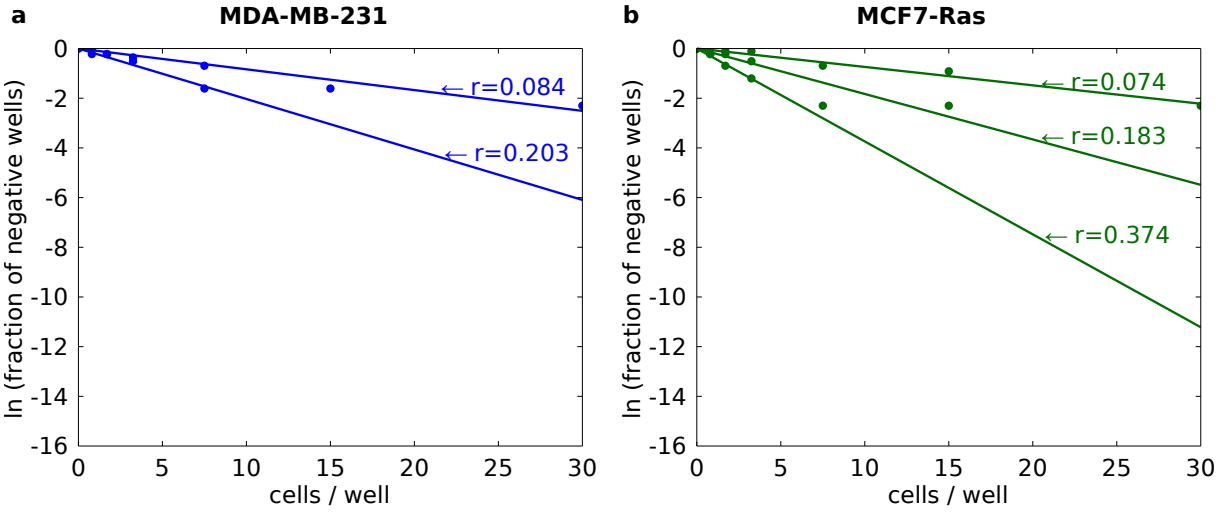

Figure 13: Results of the manually conducted Limiting Dilution Analyses for MDA-MB-231 (a) and for MCF7-Ras (b). The numbers pointing to the linear regression lines represent the particular sphere forming rates.

avoids determining the correct number of objects in a well manually. Live cell microscopy imaging is a good solution as the content of the wells is recorded for both the experiment start and end, which is not given by the classical sphere forming assay where only the number of mammospheres is counted. An additional feature is that the information is available for further investigation.

All in all, it is difficult to compare the results achieved on the basis of live cell microscopy with the results of the classic Limiting Dilution Analysis since the latter do not match the expectations of a higher sphere forming rate applied to MDA-MB-231 and characteristic rates for particular cell lines. All the more pleasant are the good results of the methods based on live cell microscopy as both expectations are matched.

3.2.3 Correlation Between the Cell Density and Sphere Forming Rate

Since the Limiting Dilution Analysis is based on different dilutions, it is interesting to see if the cell density has any impact on the sphere forming rate. This would disagree with the assumption that the breast cells do not influence each other in forming spheres (see Section 2.2.6).

As the wells used for the live cell microscopy images contain different cell densities unlike expected (see Figure 14a, b and Section 3.2.2), the sphere forming rates of each well are plotted against the corresponding cell density at the experiment start to search for correlations (see Figure 14c, d). Beside the huge densities (almost twice as much as expected) the difference between the two cell lines is remarkable. The densities of MDA-MB-231 are higher as the densities of MCF7-Ras, which is apparent in Figure 14a, b.

At a first glance the linear regression lines in Figure 14c, d suggest a negative correlation between the sphere forming rate and the cell density since the sphere forming rates decrease if the cell density increases except for the automatically determined values of MDA-MB-231 (dark blue). However, we find no significant correlation (all p-values $>$ 0.05). This is maybe caused by the few data points used as basis for their calculation.

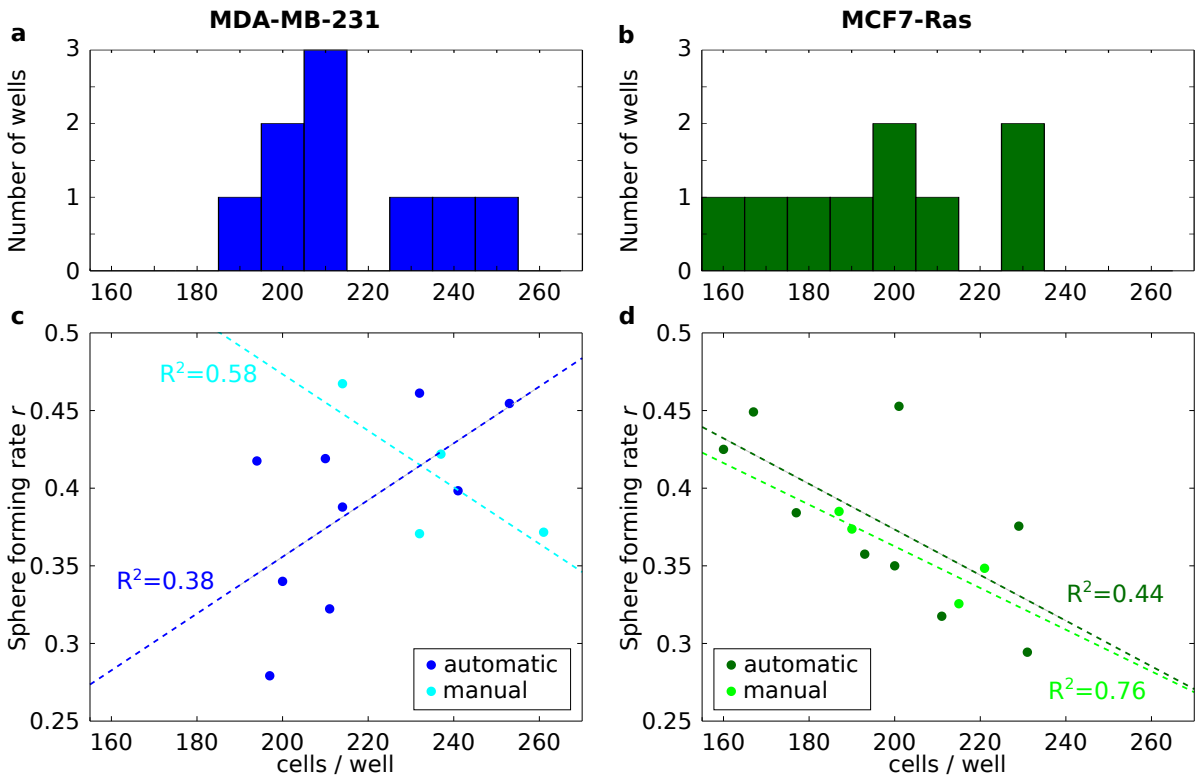

Figure 14: Sphere forming rate determined for the particular wells plotted against the corresponding cell density (c, d) and histogram of the cell densities (a, b) divided into the two cancer cell lines MDA-MB-231 and MCF7-Ras. The points in c and d are divided in the automatically and manually determined values. In addition, the linear regression lines and their corresponding R^2 values are depicted. A trend that the sphere forming rate decreases while the cell densities increase is observable especially for MCF7-Ras (d).

The R^2 values are relative small (0.38, 0.58, 0.44) except for the manually determined values for MCF7-Ras (0.76) indicating that most of the data points are far away from the linear regression curve. The high R^2 value for the automatically determined values for MCF7-Ras is not important since the regression line is not significant.

To prove or disprove a correlation between the sphere forming rate and the cell density further experiments have to be conducted and analysed.

3.3 CellProfiler Usage Evaluation

As this is the first approach of expanding CellProfiler in our group, a concluding evaluation of the usage of CellProfiler and its extension is reasonable. The following items are ranked by importance.

⊕ Since helpful explanations of CellProfiler's class structure and general workflow are provided, developing new modules is comfortable.

⊕ Once a developer environment is set up, CellProfiler's class structure is easy to understand and the provided abstract classes and inheritance hierarchy is helpful so that easy modules can be implemented fast. Since Python is a very readable

language, the code is comprehensible even for someone who is not familiar with it.

⊙ For C++-extensions experience in this language is very helpful, even if the C++ code exists already. Implementing the Cython code is not difficult, but compiling hides some difficulties in combination with OS X Mountain Lion. If all difficulties are solved once, it is comfortable to reproduce it for other extensions using the existing code as template.

⊕ Apart from the developer view, CellProfiler provides a lot of well implemented, useful modules, which have to be detected in the bulk. Handling the created pipelines is very simple since the pipelines can be stored and loaded again, which also enables sharing pipelines with colleagues.

⊖ The way to get a working development installation is not that easy due to the high number of dependencies and frameworks that are needed (see Section 3.1.2). Especially on OS X Mountain Lion, on which this study was conducted, several problems arise during installation and workarounds are difficult to find in the help pages or community forums.

⊖ One disadvantage is that CellProfiler does not work robustly all the time, e.g. sometimes it was not possible to initialise the pipeline after changing parameters after the pipeline was processed before. This might be caused by our developer version in combination with OS X Mountain Lion.

⊕ The CellProfiler developers offer support for both problems with the application and implementation within the forum [18].

⊖ It is not possible to see the effect of parameter changes during pipeline creating, instead the pipeline has to be processed until those effects can be discovered.

All in all, CellProfiler is definitely worth a try, also represented by its frequent usage [16]. It is not as robust as e.g. Fiji/ImageJ but has other advantages not offered by similar programs like the module based pipeline system coming up with an intuitive user interface. Besides it is very practical that CellProfiler stores all measurements in a single file that can be analysed simply. Getting started with the development of new modules takes time, but once set up it is quite easy.

4 Summary and Outlook

Within this thesis we created a CellProfiler pipeline for the automatic analysis of live cell microscopy images showing breast cells at the beginning of the experiment and mammospheres at the endpoint in order to determine the cell's sphere forming rate. A new CellProfiler module called *Mser* was created for the bright field segmentation.

The pipeline was applied to a live cell microscopy experiment from the Scheel lab comprising 18 wells and therefore 216 images for both experiment start and end. One half of the wells contained the more aggressive, mesenchymal cancer cell line MDA-MB-231 and the other half the epithelial cancer cell line MCF7-Ras. The performance of the pipeline was validated by manually counting of the cells and mammospheres of eight wells resulting in f-measures of 0.83 and 0.89 for the application to the images of the experiment start and the experiment end, respectively. While determining the sphere forming rates for these two cell lines by the traditional Limiting Dilution Analysis was not able to point out a difference in the sphere forming rates of the two cell lines, both the manual and the automatic approach based on live cell microscopy obtained a higher sphere forming rate for MDA-MB-231 than for MCF7-Ras as expected.

Despite the good f-measures, the new method also comprised some drawbacks since a lot of debris was found and objects were missed especially for the application of the pipeline to the images of the experiment start. As this was the first try analysing live cell microscopy images of breast cells in the mammosphere assay, room for improvement remains and the analyses show that the general approach points into the right direction. During development, several ideas for improvements came up covering different contexts, which are described in the following.

- Since our method enables the computation of one rate per well, the whole well plate can be used achieving several rates with a higher guarantee of the same conditions as if using different well plates for each rate. It is also possible to use a single well plate to calculate the sphere forming rates for several cell lines or cell lines cultured under different conditions as we did for MDA-MB-231 and MCF7-Ras. This makes the results much more comparable than using several well plates for each rate.

- The pipelines' parameter settings are determined by trial and error. Certainly better parameter settings exist, but they are hard to find. Hence, a machine learning based method to determine the parameters automatically would be preferable. This could be achieved by incorporating an active learning approach, which proposes different segmentation results to the user, who decides interactive, which result is the best, so that the parameters are learned by this choice.

- Since the cells are not adherent and therefore able to move, it is not guaranteed that the mammospheres originate from single breast cells and not through aggregation. Cell colonies caused by aggregation are not of interest and would lead to higher sphere forming rates by mistake. Therefore, operating on time-lapse movies, i.e. the images of each time point of the experiment, in combination with automatic tracking, i.e. following cells over time, promises more accurate results in determining the cells' fate i.e. death, aggregation, or forming mammospheres.

- At the moment, different parameter settings are used, but a uniform setting would be preferable. Otherwise, the parameter setting has to be adjusted if using time-lapse

movies since the object sizes grow over time and several parameters are dependent on the objects' sizes. If an aforementioned active learning of the parameters would be available determining a uniform parameter setting would be easier. In addition tracking is connected to the problem of changing object sizes so that the active parameter learning would improve the realisation of tracking as well.

- Using all images of the time-lapse movies would lead to very long processing times. Therefore, batch processing allowing parallel computing would be a good solution. CellProfiler provides a module that supports batch processing and the pipeline file can be processed over the command line headless [15]. The issue arising in this context is that CellProfiler has to be installed on a computer. Having a user interface for processing the entire batch mode would be valuable especially for researchers without computational background.

- At the moment the post-processing including the elimination of images containing large air inclusions and the computation of the sphere forming rates is done separately from CellProfiler using Matlab. It would be helpful to have a CellProfiler module that calculates the rates after the objects are identified. This module would have to provide an interactive user interface that enables the selection and deselection of images including large air inclusions so that they are not considered in computing the sphere forming rate. Furthermore, it would be necessary to decide between images belonging to particular cell lines and experimental conditions.

- Another possibility than excluding images containing large air inclusions is the calculation of the well's border to subtract this area from the raw image. Not only the well's border but also the air inclusion would be detected.

- A better background correction and therefore a better object identification especially at the wells' border might be achieved by the background correction method developed by Schwarzfischer et al. [51]. An implementation in C++ is available and could be included as an additional module into CellProfiler using Cython.

- An approach that goes in another direction is the use of out-of-focus images since segmentation sometimes works better as observed in the images of the wells' center, which mostly are out-of-focus [12]. Since debris is on another layer as the objects, it may is not visible in out-of-focus images.

- On the experimental side it could be tried to minimize the amount of debris in the wells as well as the air inclusions. This would lead to a smaller number of falsely identified objects and therefore to a better precision. A better recall could be achieved by a better illumination so that the part of the well near the well's border would be brighter and object identification would work more robust.

Taken together, the expandability on the computational side as well as the improvement opportunities on the biological side show that the analysis of breast cells with the help of live cell microscopy has wealth of feasibilities and therefore a promising future. Since this was the first time of conducting live cell microscopy and analysing the resulting images in the context of breast cells in our labs, it is necessary to analyse further live cell microscopy experiments using more wells in order to prove the method and its underlying pipeline. Nevertheless, this first application of our method provides good results pointing out a great potential. This thesis is a first step on the way to a fully automatic method for determining the sphere forming rate of breast cells in a high-throughput manner.

References

[1] Cython. http://cython.org, August 2013.

[2] GitHub CellProfiler. https://github.com/CellProfiler/CellProfiler/tree/2_0_bugfix, August 2013.

[3] Python. http://www.python.org, September 2013.

[4] Michael D. Abràmoff, Iowa Hospitals, Paulo J. Magalhães, and Michael Abràmoff. Image Processing with ImageJ.

[5] Stéphane Ansieau. EMT in breast cancer stem cell generation. *Cancer letters*, 338(1):63–8, May 2012.

[6] Carlos Arteta, Victor Lempitsky, Alison J. Noble, and Andrew Zisserman. Learning to detect cells using non-overlapping extremal regions. *Medical image computing and computer-assisted intervention : MICCAI ... International Conference on Medical Image Computing and Computer-Assisted Intervention*, 15(Pt 1):348–56, January 2012.

[7] ATCC®. MCF7 (ATCC® HTB-22™). http://www.lgcstandards-atcc.org/products/all/HTB-22.aspx?geo_country=de, September 2013.

[8] ATCC®. MDA-MB-231 (ATCC® HTB-26™). http://www.lgcstandards-atcc.org/products/all/HTB-26.aspx?geo_country=de, September 2013.

[9] Bitplane. Imaris. http://www.bitplane.com/go/products/imaris, August 2013.

[10] Breastcancer.org. Types of Breast Cancer. http://www.breastcancer.org/symptoms/types, August 2013.

[11] Felix Buggenthin. Computational prediction of hematopoietic cell fates using single cell time lapse imaging. Diplomarbeit, Ludiw-Maximilians-Universität and Technischen Universität München, Munich, Germany, 2011.

[12] Felix Buggenthin, Carsten Marr, Michael Schwarzfischer, Philipp S. Hoppe, Timm Schroeder, and Fabian J. Theis. An automatic method for robust and fast cell detection in bright field images from high-throughput microscopy. *to be published in BMC*, 2013.

[13] Statistisches Bundesamt. Todesursachen. https://www.destatis.de/DE/ZahlenFakten/GesellschaftStaat/Gesundheit/Todesursachen/Tabellen/SterbefaelleInsgesamt.html, August 2013.

[14] Anne E. Carpenter, Thouis R. Jones, Michael R. Lamprecht, Colin Clarke, In Han Kang, Ola Friman, David A. Guertin, Joo Han Chang, Robert A. Lindquist, Jason Moffat, Polina Golland, and David M. Sabatini. CellProfiler: image analysis software for identifying and quantifying cell phenotypes. *Genome biology*, 7(10):R100, January 2006.

[15] CellProfiler. Batch Processing. http://www.cellprofiler.org/CPmanual/Help_Using%20CellProfiler_Other%20Features_Batch%20Processing.html, September 2013.

[16] CellProfiler. CellProfiler citations. http://www.cellprofiler.org/citations.shtml, August 2013.

[17] CellProfiler. CellProfiler developer's version installation for Mac. http://github.com/CellProfiler/CellProfiler/wiki/CellProfiler-developer's-version-installation-for-Mac, September 2013.

[18] CellProfiler. CellProfiler forum. http://cellprofiler.org/forum/, August 2013.

[19] CellProfiler. Module: EnhanceOrSuppressFeatures. http://www.cellprofiler.org/CPmanual/EnhanceOrSuppressFeatures.html, August 2013.

[20] CellProfiler. Module: FilterObjects. http://www.cellprofiler.org/CPmanual/FilterObjects.html, September 2013.

[21] CellProfiler. Module: IdentifyPrimaryObjects. http://www.cellprofiler.org/CPmanual/IdentifyPrimaryObjects.html, September 2013.

[22] CellProfiler. Module: ImageMath. http://www.cellprofiler.org/CPmanual/ImageMath.html, September 2013.

[23] CellProfiler. Module: LoadImages. http://www.cellprofiler.org/CPmanual/LoadImages.html, September 2013.

[24] CellProfiler. Module: MeasureObjectSizeShape. http://www.cellprofiler.org/CPmanual/MeasureObjectSizeShape.html, September 2013.

[25] CellProfiler. Module: SaveImages. http://www.cellprofiler.org/CPmanual/SaveImages.html, September 2013.

[26] CellProfiler. Module Structure and Data Storage Retrieval. https://github.com/CellProfiler/CellProfiler/wiki/Module-Structure-and-Data-Storage-Retrieval, August 2013.

[27] Christine L. Chaffer and Robert A. Weinberg. A perspective on cancer cell metastasis. *Science (New York, N.Y.)*, 331(6024):1559–64, March 2011.

[28] CellProfiler Community. equal sign in identifyprimaryobjects.py. http://cellprofiler.org/forum/viewtopic.php?f=16&t=3435, September 2013.

[29] Molecular Devices. MetaXpress. http://www.moleculardevices.com/Products/Instruments/High-Content-Screening/MetaXpress-Software.html, August 2013.

[30] Gabriela Dontu, Wissam M. Abdallah, Jessica M. Foley, Kyle W. Jackson, Michael F. Clarke, Mari J. Kawamura, and Max S. Wicha. In vitro propagation and transcriptional profiling of human mammary stem/progenitor cells. *Genes & Development*, 17(10):1253–1270, 2003.

[31] Gabriela Dontu and Max S. Wicha. Survival of mammary stem cells in suspension culture: implications for stem cell biology and neoplasia. *Journal of mammary gland biology and neoplasia*, 10(1):75–86, January 2005.

[32] Max Endele and Timm Schroeder. Molecular live cell bioimaging in stem cell research. *Annals of the New York Academy of Sciences*, 1266:18–27, August 2012.

[33] NetDoktor.de GmbH. C50 - Bösartige Neubildung der Brustdrüse (Mamma). http://www.netdoktor.de/Service/ICD-Diagnose/C50-Boesartige-Neubildung-der-40214.html, August 2013.

[34] Lothar Hennighausen and Gertraud W. Robinson. Signaling Pathways in Mammary Gland Development. *Developmental Cell*, 1(4):467–475, October 2001.

[35] Yifang Hu and Gordon K. Smyth. ELDA: extreme limiting dilution analysis for comparing depleted and enriched populations in stem cell and other assays. *Journal of immunological methods*, 347(1-2):70–8, August 2009.

[36] National Cancer Institute. Definition: invasive cancer. http://www.cancer.gov/Common/PopUps/popDefinition.aspx?id=45741, September 2013.

[37] Lee Kamentsky, Thouis R. Jones, Adam Fraser, Mark-Anthony Bray, David J. Logan, Katherine L. Madden, Vebjorn Ljosa, Curtis Rueden, Kevin W. Eliceiri, and Anne E. Carpenter. Improved structure, function and compatibility for CellProfiler: modular high-throughput image analysis software. *Bioinformatics (Oxford, England)*, 27(8):1179–80, April 2011.

[38] Ivan Lefkovits and Herman Waldmann. *Limiting dilution analysis of cells of the immune system.* Oxford University Press, Oxford, 2nd edition, 1999.

[39] Peihong Ma, Maureen Magut, Xinbin Chen, and Chang-yan Chen. p53 Is Necessary for the Apoptotic Response Mediated by a Transient Increase of Ras Activity p53 Is Necessary for the Apoptotic Response Mediated by a Transient Increase of Ras Activity. *Molecular and Cellular Biology*, 22(9):2928–2938, 2002.

[40] J. Matas, O. Chum, M. Urban, and T. Pajdla. Robust wide-baseline stereo from maximally stable extremal regions. *Image and Vision Computing*, 22(10):761–767, September 2004.

[41] MathWorks. Boxplot. http://www.mathworks.de/de/help/stats/boxplot.html, September 2013.

[42] MathWorks. mad. http://www.mathworks.de/de/help/stats/mad.html, September 2013.

[43] MathWorks. Matlab. http://www.mathworks.de/products/matlab/, August 2013.

[44] Mark S. Nixon and Alberto S. Aguado. *Feature Extraction & Image Proscessing for Computer Vision.* Academic Press as an imprint of Elsevier, United Kingdom, 3rd edition, 2012.

[45] Nobuyuki Otsu. A threshold selection method from gray-level histograms. *IEEE Transactions on Systems, Man, and Cybernetics*, 9(1):62–66, 1979.

[46] Derek C. Radisky, Yohei Hirai, and Mina J. Bissell. Delivering the message: epimorphin and mammary epithelial morphogenesis. *Trends in Cell Biology*, 13(8):426–434, August 2003.

[47] Genetics Home Reference. HRAS. http://ghr.nlm.nih.gov/gene/HRAS, September 2013.

[48] Tannistha Reya, Sean J. Morrison, Michael F. Clarke, and Irving L. Weissman. Stem cells, cancer, and cancer stem cells. *Nature*, 414(6859):105–11, November 2001.

[49] Lauren M Rota, Deborah A. Lazzarino, Amber N. Ziegler, Derek LeRoith, and Teresa L. Wood. Determining mammosphere-forming potential: application of the limiting dilution analysis. *Journal of mammary gland biology and neoplasia*, 17(2):119–23, June 2012.

[50] Timm Schroeder. Long-term single-cell imaging of mammalian stem cells. *Nature methods*, 8(4 Suppl):S30–5, April 2011.

[51] Michael Schwarzfischer, Carsten Marr, Jan Krumsiek, Philipp S. Hoppe, Timm Schroeder, and Fabian J. Theis. Efficient fluorescence image normalization for time lapse movies. *unpublished*, pages 1–5, 2011.

[52] Anurag Singh and Jeffrey Settleman. EMT, cancer stem cells and drug resistance: an emerging axis of evil in the war on cancer. *Oncogene*, 29(34):4741–51, August 2010.

[53] Gleb V. Tcheslavski. Morphological Image Processing: Gray-scale morphology. `http://ee.lamar.edu/gleb/dip/10-3%20-%20Morphological%20Image%20Processing.pdf`, September 2013.

[54] Jane E. Visvader. Keeping abreast of the mammary epithelial hierarchy and breast tumorigenesis. *Genes & development*, 23(22):2563–77, November 2009.